



Serviço Público Federal

Ministério da Educação

Fundação Universidade Federal de Mato Grosso do Sul
Programa de Pós-Graduação em Tecnologias Ambientais



**FLOW DISTRIBUTION AND MASS REMOVAL IN A FLOATING
TREATMENT ISLAND WITH DIFFERENT DEPTHS IN A CHANNEL
CAVITY**

Felipe Rezende da Costa

CAMPO GRANDE – MS

October/2023

Federal University of Mato Grosso do Sul
College of Engineering, Architecture and Urbanism and Geography
Graduation Programme in Environmental Technologies

Felipe Rezende da Costa

FLOW DISTRIBUTION AND MASS REMOVAL IN A FLOATING
TREATMENT ISLAND WITH DIFFERENT DEPTHS IN A CHANNEL
CAVITY

A dissertation submitted in fulfillment of the requirements for the Master of Science degree in the Graduation Programme in Environmental Technologies in the Federal University of Mato Grosso do Sul, academic area: Environmental Sanitation and Water Resources

Advisor: Prof. Dr. Johannes Gérson Janzen

Approved in:

Dissertation Committee:

Prof. PhD. Johannes Gérson Janzen
President

Prof. PhD. Paulo Henrique Silva de Lima

PhD. Manoel Lucas Machado Xavier

Campo Grande, MS

Dedication

To my parents, Fabrízio and Priscila, for always supporting me and doing everything they could to enable me to follow this path.

To my brother João Victor for always being my partner and always waking up with me before the sun rises to start the day.

To all my friends who were with me and fought the battles with me from high school, through university until I ended up here.

To all colleagues and former colleagues at the UFMS CFD laboratory, for the good times and learning.

To Professor Johannes Janzen, advisor, for teachings, advice and discussions.

I will always be grateful for everything. To the entire team of technicians and teachers at FAENG and PGTA at UFMS.

Table of Contents

1. Introduction.....	4
2. Numerical Model.....	7
2.1. Model Equations.....	7
2.2. Numerical Model.....	9
3. Results and Discussion.....	16
3.1. Flow hydrodynamics.....	17
4. Conclusion.....	39
Declaration of Competing Interest.....	41
Acknowledgements.....	41
References.....	41

Flow distribution and mass removal in a floating treatment island with different depths in a channel cavity

Family Name: da Costa, Given Name: Felipe Rezende; felipe.costa@ufms.br
(Corresponding Author)¹

Family Name: Janzen, Given Name: Johannes Gérson; johannesjanzen@gmail.com¹

Affiliations:

1 – Faculty of Engineering, Architecture and Urban Planning, and Geography, Federal University of Mato Grosso do Sul, Campo Grande, Brazil

Corresponding Author Full Postal Address: Laboratório 6, Unidade 11, Universidade Federal de Mato Grosso do Sul, Av. Costa e Silva, s/nº, Bairro Universitário, 79070-900, Campo Grande, Mato Grosso do Sul, Brazil

Abstract

In open rivers and canals, lateral cavities are adjacent regions that affect flow, creating a water recirculation zone and reducing flow energy and with that they provide the retention of sediments, the protection of riverbanks and refuge for organisms that develop in calmer waters. The presence of vegetation in these structures offers additional resistance to flow which affects the magnitude of flow-related variables, for example, intensifying the deceleration inside the cavity and impacting mass exchange processes between the main channel and the dead zone. This study evaluated the hydrodynamic interactions effect of floating vegetation

within the lateral cavity on the circulation system using Computational Fluid Dynamics (CFD) and laboratory experiments. In the simulations, the anisotropic resistance generated by the vegetation was represented by a porous zone, this is a simple, way to represent this resistance exerted to the flow, and yet effective in capturing the effects on hydrodynamics. Vegetation density remained constant and had 5 different vegetation depths studied in the simulations and for initial practical tests only one vegetated case was used. In all simulated cases, the presence of floating vegetation reduced the magnitude of the velocity in the innermost part of the cavity compared to areas without vegetation, while in the laboratory cases there was almost absolute deceleration in most of the vegetated region with points of acceleration. Increasing the depth of vegetation decreased the flow velocity in the lateral cavity, reaching its maximum effect in a case of a fully filled cavity.

Keywords: Dead water zones (DWZ); Open Channel; Computational Fluid Dynamics (CFD).

1. Introduction

Natural river ecosystems are characterized by intricate boundaries, including dead-water zones (DWZs) formed by embayments or consecutive groins located on the banks of a river, which can be generated naturally or artificially. In these zones, the mean velocity is comparatively lower than the main channel due to energy absorption of the main channel flow, fostering increased lateral heterogeneity (WEITBRECHT; SOCOLOFSKY; JIRKA, 2008) and are important elements that make up the geometry of rivers (JACKSON et al. 2013).

Furthermore, these structures provide conducive conditions for the proliferation of aquatic organisms, thereby enriching the biodiversity of river ecosystems (ASAEDA et al., 2009). This environment also mitigation of bank erosion by facilitating the deposition and temporary storage of suspended sediment (JUEZ et al., 2018), favoring growth of vegetation (ASAEDA et al., 2009) and refuge for aquatic organisms (JACKSON et al. 2013; XIANG et al. 2019). Added to this, the DWZ also accumulate pollutants, leading to influence on river systems by enhancing water quality by removing these pollutants from the main channel and controlling pollutant dissipation, while offering the potential for pollutant purification by the biota inhabiting DWZs (LIU and LU, 2013; XIANG et al., 2019).

An alternative approach for pollutant removal in DWZs involves the use of floating treatment wetlands (FTWs). Operating similarly to hydroponic systems, FTWs utilize direct root-water column contact to facilitate the uptake of nutrients, aided by the growth of microbial biofilms on the root mass, thereby enhancing nutrient removal and establishing a mutualistic relationship with the FTW plant species (HEADLEY and TANNER, 2006; BI et al., 2019). Furthermore, the roots serve as a porous barrier, enhancing physical removal through filtration and sedimentation (SCHWAMMBERGER et al., 2019; HEADLEY and TANNER, 2012). FTWs also provide additional ecological benefits, such as serving as habitats for diverse fauna, including waterfowl, amphibians, and reptiles (HUANG et al., 2017; YAMAKI and YAMAMURO, 2013; HANCOCK, 2010; CAZZANELLI et al., 2008).

Regarding vegetated cavities, there are few studies that investigate them, whether the vegetation is emerging or submerged. The presence of regions with low-velocity flow can promote an increase in sedimentation rates, enabling the availability of nutrients for the development of vegetation (SUKHODOLOV, 2014). The flow

characteristics in a vegetated lateral cavity depend on the main channel flow, cavity geometry and vegetation characteristics (XIANG et al. 2019; XIANG et al. 2020; Oliveira, 2021).

In the realm of FTWs, hydrodynamics assumes a critical role, influencing the removal performance by regulating both the pollutant mass flux entering each FTW root zone and the residence time of fluid and pollutant mass within these zones. The optimization of hydrodynamic conditions within FTWs is essential to ensure effective pollutant removal and system efficiency (Nuruzzaman et al., 2021; Liu et al., 2019; Lucke et al., 2019; Xavier et al., 2018). Additionally, the geometric aspects of FTWs, such as root length, significantly impact the total reactive volume and the fraction of pollutant inflow entering the root zone. While an increased root length may enhance pollutant removal by allowing a higher fraction of pollutant inflow to pass through the root zone, it can also elevate the velocity, thereby reducing the residence time and potentially mitigating the improvement in removal.

Through the growth of vegetation, there are changes in the hydrodynamics of the region, making the density and position of vegetation become relevant factors. However, the study of the effect on hydrodynamics caused by floating vegetation is even scarcer. Hydrodynamics is one of the basic properties within the classification based on the hydro geomorphic functions of wetlands (BRINSON, 1993) while the study of floating vegetation becomes important because it is vegetation naturally transported and present in aquatic environments. Floating vegetation can be used as a filter for sediments brought by runoff (NICHOLS et al. 2016) and for the biological treatment of pollutants (LI et al. 2009).

Considering the importance of constructed floating wetland systems, in showing high capacity to deal with different types of pollutants. It is noted that a constructed floating wetland system (SFWC) consists of a structure of floating material, which houses emerging macrophytes, guaranteeing buoyancy to the system (WERAGODA et al., 2012) Regarding vegetation in the processes that occur inside a cavity, little is known about its influence, especially with regard to sediment transport (OLIVEIRA et al. 2022). In this way, given the under explored implementation of FTWs in cavities, the present study employs numerical experiments to investigate how root length influences flow distribution and mass removal in this context.

2. Numerical Model

2.1. Model Equations

The Large Eddy Simulation (LES) method was used as the turbulence model for simulation, a method that uses the Navier-Stokes equation to calculate fluid detachment and turbulence . Considering incompressible flow to filter the equation (Equation 1), the filtered continuity equation (Equation 2) is obtained.

$$\frac{\partial \bar{u}_i}{\partial x_i} = 0 \quad (1)$$

$$\frac{\partial \bar{u}_i}{\partial t} + \frac{\partial}{\partial x_j} (\bar{u}_i \bar{u}_j) = -\frac{1}{\rho} \frac{\partial \bar{p}}{\partial x_i} + \frac{\partial}{\partial x_j} [\mu (2\bar{S}_{ij}) - \tau_{ij}] + \bar{S}_{M,i} \quad (2)$$

where the over bar indicates calculated values, u_i (m/s) is the velocity component in direction i and j ($i = 1, 2, 3$ corresponding to the x, y, z axes, respectively), ρ (kg/m³) is the density of the fluid, p (N/m²) is the dynamic pressure, μ (m²/s) is the kinetic viscosity, S_{ij} (1/s) is the strain rate tensor, τ_{ij} (m²/s²) is the subgrid scale tensor, and $S_{M,i}$ is the effect of the vegetation drag coefficient. S_{ij} and τ_{ij} are calculated by:

$$\bar{S}_{ij} = \frac{1}{2} \left(\frac{\partial u_i}{\partial x_j} + \frac{\partial u_j}{\partial x_i} \right) \quad (3)$$

$$\tau_{ij} = \bar{u}_i \bar{u}_j - \overline{u_i u_j} \quad (4)$$

Since the model is based on an assumption of eddy-viscosity, τ_{ij} can be represented by:

$$\tau_{ij} - \frac{1}{3} \tau_{kk} \delta_{ij} = -\vartheta_t (2\bar{S}_{ij}) \quad (5)$$

In which ϑ_t (m²/s) is the eddy viscosity, to solve it the subgrid-scale Wall-Adapting Local Eddy-viscosity (WALE), as developed by Nicoud and Ducros (1999).

The advection-diffusion equation (ADE) (equation 6) was employed to simulate the conveyance of scalars. This equation incorporates a unidirectional interaction with the flow, meaning that the flow remains unaffected by the scalar transport.

$$\frac{\partial C}{\partial t} - \nabla \cdot (UC) - \nabla^2 (D_T C) = 0 \quad (6)$$

whitch C is the tracer concentration, ranging from 0 to 1 to represent tracer concentration, and $D_T = 1.111$ is the constant diffusion coefficient divided by the fluid density.

2.2. Numerical Model

The geometry of the initial situation consisted of a channel region with a side cavity (Figure 1) based on the laboratory experiment by Xiang et al. (2019). It consisted of a channel 1.25m long and 0.30m wide, the cavity was 0.25m long and 0.15m wide and both were 0.10m deep. The average velocity in the main channel was constant and maintained at $U = 0.101\text{m/s}$, which results in a turbulent ($Re = HU/\nu = 9000$, where ν is the kinematic viscosity) and subcritical flow ($Fr = U/(gH)^{0.5} = 0.102$, where g is the gravitational acceleration) at a temperature of 293K.

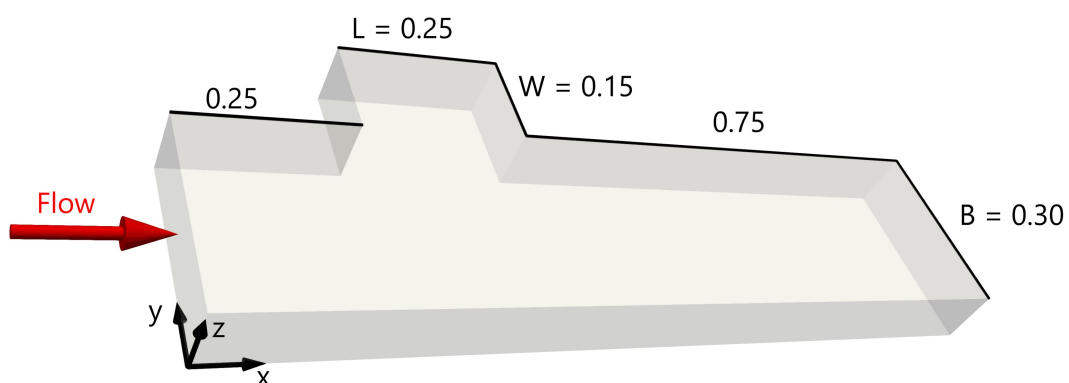


Figure 1 - Computational domain with coordinates, sizes and main boundary conditions. All the sizes are in metres

The origin of the coordinate axis is found in the main channel cavity interface, in the most upstream point of the cavity and at the bottom of the channel. The boundary conditions on the free surface ($z = 0.10\text{m}$) was sliding wall, simplification practice in CFD for $Fr < 0.36$ (Khosronejad et al., 2020). This is a simulation used in open channel simulations with Froude number values less than 0.43 (Lu and Dai, 2016; Ouro et al., 2020; Xiang et al., 2019). Although the use of the Level-Set Method (LSM) generates better precision at the air-water interface, this condition generates up to 5 times more computational consumption (Khosronejad et al., 2020) with the rigid-lid assumption obtaining results of first- order turbulence statistics consistent with experimental ones (Kara et al., 2015). For the longitudinal XZ plane far field ($y = -0.30\text{m}$) was set as sliding wall condition, simplification that is valid since the main channel flow does not affect the development of transverse standing waves

. The channel entrance ($x = -0.25\text{m}$) had the velocity field previously fully developed, with initial flow conditions ($U = 0.101\text{ m/s}$), in periodic domain simulation with the same conditions and geometry as the main channel). The exit plane ($x = 1.0\text{m}$) was configured as a zero gradient region, to guarantee the exit of the flow without return flow. The domain bed and the side walls of the main channel and cavity were configured as non-sliding walls, corresponding to a system characterized by a single gyre, accompanied by a neighboring circulation

. The width of the main channel was set to twice the width of the cavity, which represented a smaller domain than that performed by Xiang et al. (2019), resulting in a reduction from 0.85 m to 0.30 m. This reduction was chosen to reduce computational consumption by reducing the domain and eliminating the need to resolve the boundary layer near the region of the wall opposite the cavity. This simplification was possible because it is a region where, in addition to no longer

having significant effects from the cavity (Brevis et al., 2014), the flow is already parallel and mostly uniform, which generates a region where the free-slip symmetry condition can be applied.

To run the simulation, the open source software OpenFOAM (version 2212) was used. The turbulence model chosen was the Large eddy simulation (LES) and to provide the necessary precision for the model, second order numerical schemes were used. These decisions were taken to guarantee dependable forecasts of transport phenomena, especially in situations where scalar quantities exert a substantial influence. The pimpleFoam module consisting of the finite volume method was chosen to generate the mesh and discretize the numerical schemes and governing equations, an efficient module for implementation of the finite volume method (FVM) in a transient formulation. By employing this method, we were able to precisely capture the dynamic characteristics of the flow and its interactions with the surrounding environment. To solve the pressure-velocity coupling, the PIMPLE method was chosen, which combines the transient and permanent formulations of PISO and SIMPLE, respectively. Opting for this selection facilitated the attainment of a resilient and steady convergence in both the pressure and velocity fields, a crucial factor for ensuring precision in the flow simulation.

The unique characteristics of our numerical model compared to the approach introduced by Xiang et al. (2019) are highlighted by several factors. These include the implementation of additional corrective measures, the utilization of a porous medium to achieve mesh orthogonality, and the development of a distinct inlet boundary condition. Moreover, our model's dependence on openly accessible software contrasts with the previous reliance on proprietary solutions, marking a significant departure from traditional methodologies.

The implementation of a tracer removal procedure, instant tracer injection into the study volume, within the side cavity was used to simulate mass discharge between the main channel and the cavity (Equation 6). After time $150 H/U$ seconds (water depth $H = 0.10\text{m}$, and channel bulk velocity $U = 0.101\text{ m/s}$), enough time to develop flow and eliminate flow transients, the tracer was inserted into the cavity with concentration $C = 0$ in the main channel and $C = 1$ inside of the vegetation in the cases 1 to 5 and inside the whole cavity for case 0, case without vegetation. The flow was averaged for an additional 200 seconds, enough time for the concentration within the measured region to drop by 95%, in which time-averaged amounts were calculated and the tracer was tracked as it exited the cavity. The Schmidt number was $S_{ct} = 0.9$; as well as in simulations with similar flows (Gualtieri et al., 2010), but it is worth highlight that the turbulent Schmidt number on the mass exchange of a vegetated lateral cavity is almost negligible, since doubling the S_{ct} changes the mass exchange by 1% .

The Courant number was adaptive, however, below 0.90 and the time step below 0.05s, with the mean time step size of 0.001s. The residual velocity and pressure tolerance was set to 1E-04. All simulations ran for $350H/U$ seconds, where the first $150H/U$ seconds were for eliminating transients and the remaining $200H/U$ seconds statistics were collected and averaged using the instantaneous flow fields.

The representation of vegetation in CFD traditionally uses several rigid cylinders inside the cavity to represent the density of vegetation and the imposed drag , resulting in a complex mesh that is difficult to calculate. Since the spaces between the cylinders are very small, the mesh needs to be very refined, which results in a very heavy mesh with great computational cost . The solution chosen for

this study was to represent vegetation as a porous Darcy-Forchheimer medium . The porous zone that represents the vegetated area had the loss of momentum computed using the Darcy-Forchheimer (DF) model (Equation 6).

$$\bar{S}_{M,i} = - \left(\mu d + \frac{\rho |u_{jj}|}{2} f \right) u_i \quad (7)$$

where μ (m²/s) is the kinematic viscosity d (1/m²) is the viscosity drag coefficient and f (1/m) is the inertial coefficient and are calculated using the Ergun equation:

$$d = \frac{150}{D_p^2} \frac{(1-\epsilon)^2}{\epsilon^3} \quad (8)$$

$$f = \frac{3.5}{D_p} \frac{(1-\epsilon)}{\epsilon^3} \quad (9)$$

in which D_p (cm) is the mean particle diameter. Since the porous medium were validated with laboratory experiments by Xiang et al. (2019), D_p was considered to be the diameter the copper wires $d_w = 1.5$ mm for the flow perpendicular to the rods (flows in the x and y axes), while in the flow parallel to the rods (flow in the z axis) the coefficients d and f were calculated using the approach of Oldham and Sturman (2001), as the resistance was non-isotropic, where the diameter dh is calculated by Equation 10.

$$d_h = d_w \left(\frac{4(s/d_w)^2}{\pi} - 1 \right) \quad (10)$$

Furthermore, ϵ ($= 1-a$) is the void fraction, where a is the vegetation density inside the cavity (Equation 11).

$$a = \frac{nS_V}{S_{cav}} \quad (11)$$

where n is the number of vegetation stems, S_V (m^2) is the area of the horizontal cross-section of the stems and S_{cav} (m^2) is the area of the cavity.

Since this study proposes to analyse the effect of varying depths of floating vegetation in the cavity, different vegetation depths were studied, in which, the same vegetation density ($a = 0.1332\%$) and homogeneous dispersion of vegetation within the occupied area was assumed. The depth range was between $z = 0h$ (no vegetation) and $z = 1.0h$ (equal depth of roots and cavities), distributed across six scenarios with its parameters shown in Table 1.

Case	z/H	Direção horizontal (eixos x e y)		Direção vertical (eixo z)		
		d (1/m ²)	f (1/m)	d _h (m)	d (1/m ²)	(1/m)
0	0	0	0	0	0	0
1	0.2	116.53	3.09	0.7624	0.00045	0.00608
2	0.4	116.53	3.09	0.7624	0.00045	0.00608
3	0.6	116.53	3.09	0.7624	0.00045	0.00608

4	0.8	116.53	3.09	0.7624	0.00045	0.00608
5	1.0	116.53	3.09	0.7624	0.00045	0.00608

Table 1 - Vegetation levels and the calculated Darcy-Forchheimer coefficients.

The quality of the numerical model was evaluated using the three-grid method (DUTTA; XING, 2018), where three meshes were generated with an effective refinement rate of 1.40 between them. The coarsest mesh had 639,680 elements, the intermediate one had 1,408,000 elements and the most refined one had 3,132,800 elements, generating an error equal to 2E-05 m/s, obtained with the method proposed by Dutta and Xing (2018). In the end, all three-grid simulated ensemble-averaged streamwise velocities showed to be in agreement with the experimental results of Xiang et al. (2019) (Figure 2).

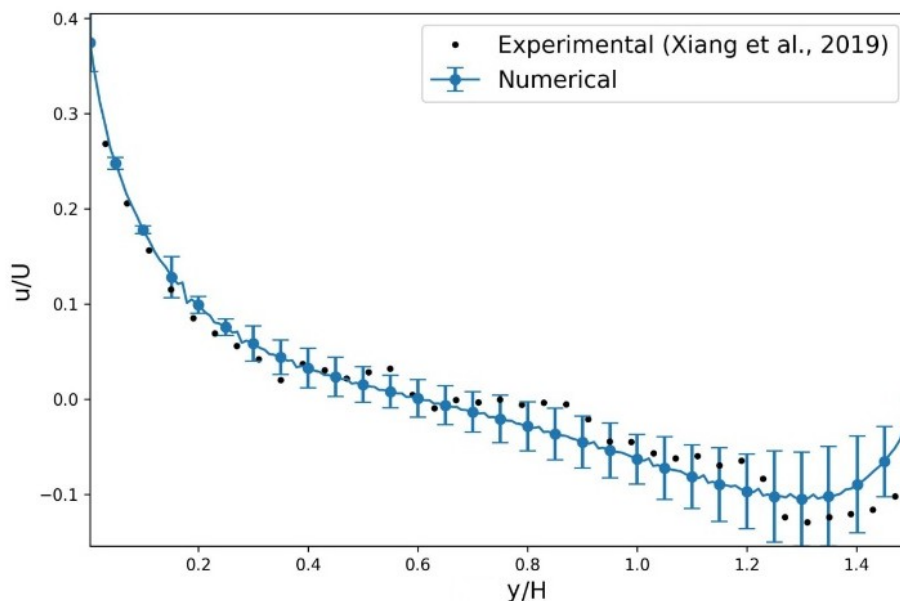


Figure 2 - Ensemble-averaged streamwise velocity in the cavity at $z/H = 0.6$ for vegetation depth $z = 1.0H$ (the x direction was spatially averaged into a single value), where U is the bulk velocity in the main channel and H is the cavity depth. $y/H = 0$ is at the interface between the lateral cavity and the main channel.

For the continuation of the tests, the intermediate mesh was chosen for the simulations, which presented 1.74% uncertainty with the experimental results. The intermediate mesh was divided into 240 elements in the flow direction (x-axis), 120 elements in the channel width direction (y-axis) and 40 elements in the vertical direction (z-axis). The cavity was discretized into 80x80x40 elements, on the x-axis, y-axis and z-axis, respectively (Figure 3). In the domain, the maximum time-averaged non-dimensional wall distances were $y^+ = 5.93$ in the spanwise direction and $z^+ = 1.99$ in the vertical direction. Correspondingly, the spatial-averaged distances were approximately $y^+_{ave} = 1.64$ and $z^+_{ave} = 0.68$. Consequently, the first grid off the wall falls within the viscous sub-layer of the domain. The simulation was calculated on 48 cores [2 x Intel Xeon E5-2670v3 (Haswell) at a base clock of 2.3 GHz].

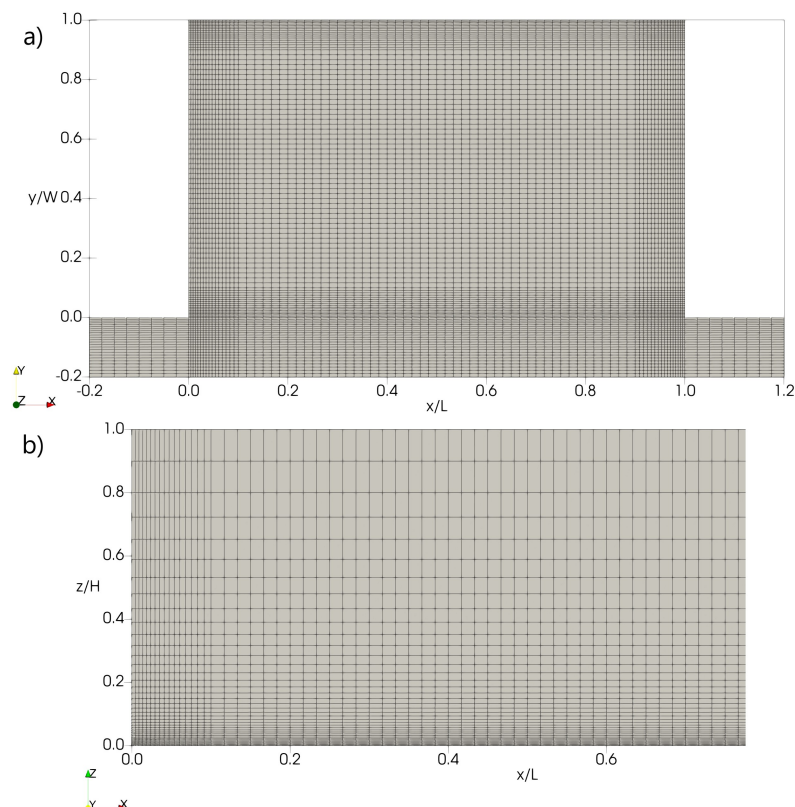


Figure 3 – Computational grid in all cases: a) mesh in the free-surface plane around the cavity and b) mesh in the vertical plane.

3. Results and Discussion

3.1. Flow hydrodynamics

Figure 4 shows streamlines of the time-averaged horizontal flow and its magnitude $\sqrt{u^2+v^2}/U$ inside the cavity at $z/H = 0.6$ for all vegetation depths, with figure 4a being the case without vegetation and the alphabetical sequence following the sequence of increasing depth of floating vegetation. Flow in the main channel occurs from left to right in all images. In all cases a counter-clockwise recirculation zone formed in the most downstream region with low speed at the center of the spin, but with a flow that accelerates as it moves away from the center. In the case without vegetation, the main vortex is also accompanied by the emergence of a smaller articulation zone but in the region further away from the interface and close to the upstream wall. This secondary vortex still remains in the case where the floating island descends to 80% of the depth (Figure 4b), however, from the point that the vegetation reaches the secondary vortex (Figure 4c-e) it dissipates. For the case with emerging fluctuation (case 5, Figure 4f), the secondary vortex appears again when the vegetation becomes emergent, that is, in the case where the flow resistance stops varying in the vertical axis. Furthermore, as the vegetation gradually becomes deeper, the velocity field follows this growth and becomes gradually slower. This process of speed reduction reaches its peak when the roots of the floating island reach the bottom of the channel (case 5, Figure 4-f), being the case that presents the speed regions with the lowest magnitude and greatest extension

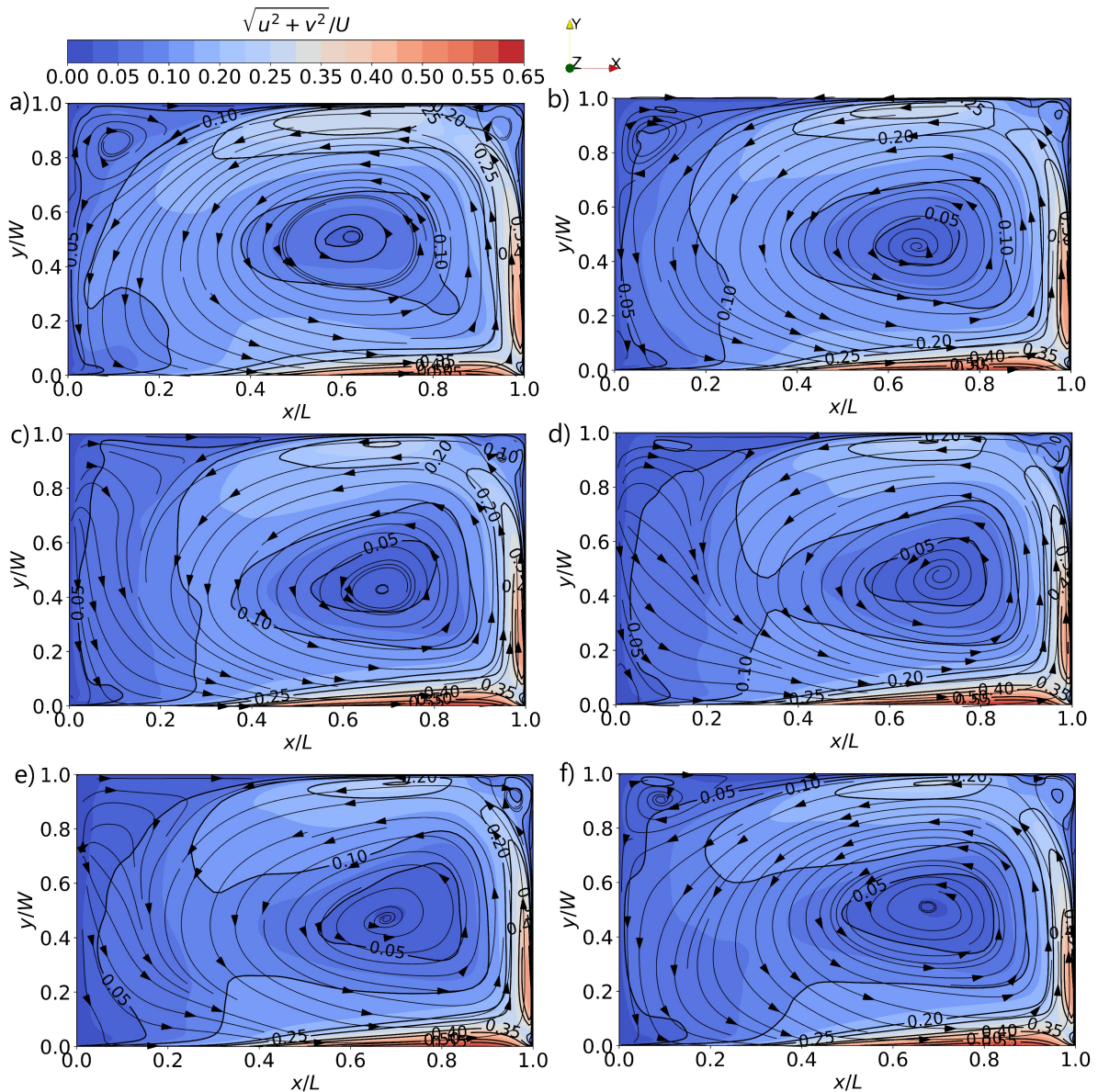


Figure 4 - Mean 2D streamlines of different vegetation densities at the horizontal plane $z/H = 0.6$ inside the cavity volume with vegetation depth of: a) $0.0H$, b) $0.2H$, c) $0.4H$, d) $0.6H$, e) $0.8H$ and f) $1.0H$.

Figure 5, as well as Figure 4, shows streamlines of the time-averaged horizontal flow and its magnitude $\sqrt{u^2 + v^2}/U$ inside the cavity, however at different depths. The figure is a comparison between the case without floating vegetation case zero and the case with floating vegetation up to 60% of the depth Case 3 where the figures on the left represent case 0 and on the right case 3 with depth $z = 0.2H$, $z = 0.5H$ and $z = 0.8H$ in Figure 5 a-b, Figure 5 c-d and Figure 5 e-f, respectively. The presence or absence of vegetation, whether floating or emergent, did not affect the heterogeneity

of the velocity profiles with depth variation. For all situations, each plane presented its velocity profile, in addition to showing trends towards slower flow as it approaches the bottom of the channel. Furthermore, the deceleration process shown in Figure 4 was repeated for the other planes, showing that the influence of floating vegetation still reaches depths without vegetation, even if on a smaller scale compared to when there is vegetation in the region.

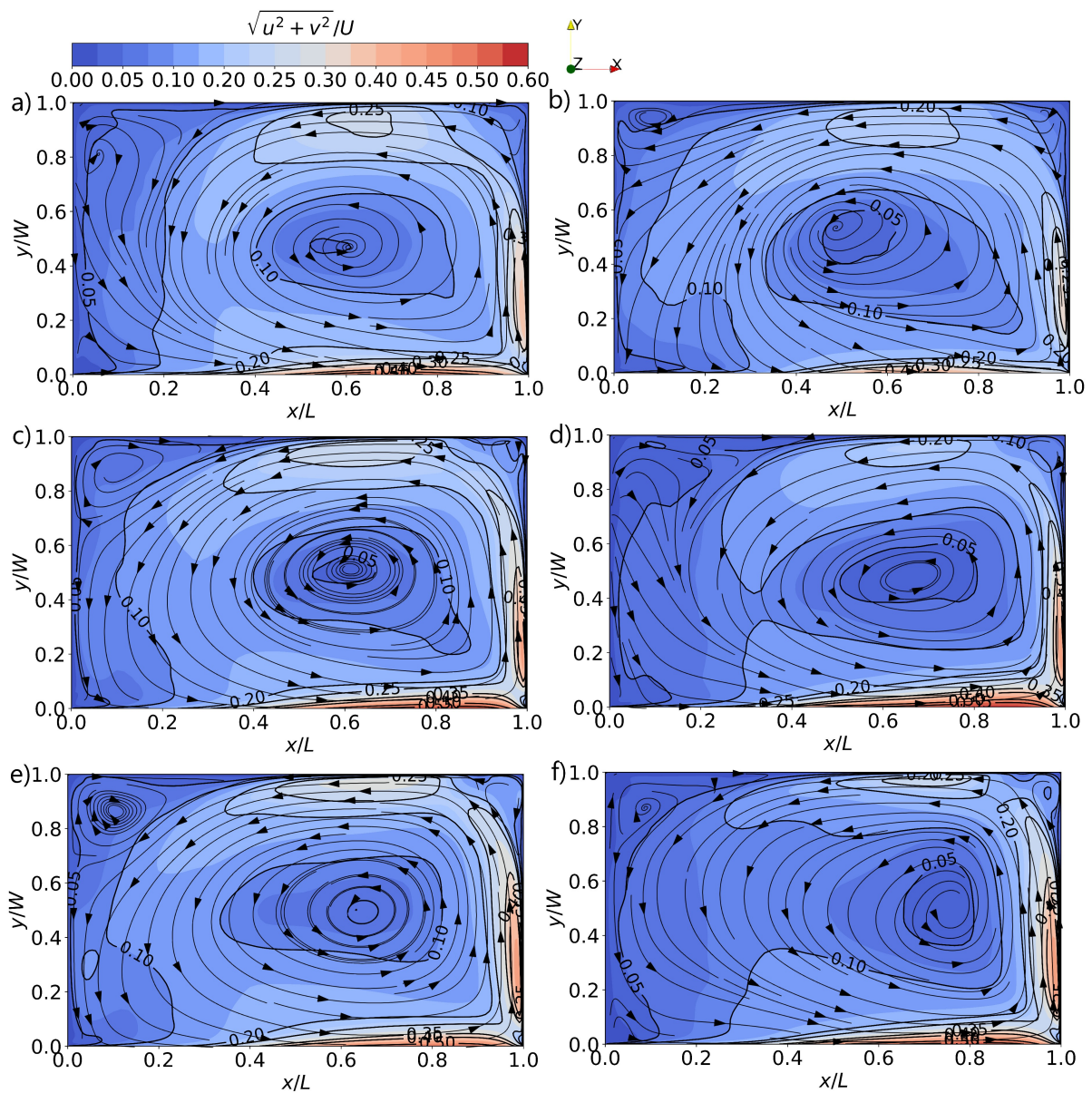


Figure 5 - Mean 2D streamlines of different vegetation densities at the horizontal plane in different depths inside the cavity volume for the case without vegetation at: a) $z = 0.2H$, c) $z = 0.5H$ and e) $z = 0.8H$, and the case with vegetation depth of $0.6H$ at: b) $z = 0.2H$, d) $z = 0.5H$ and f) $z = 0.8H$.

Figure 6 shows the velocity profiles in the vertical direction for all cases at $z = 0.6H$, following the same sequence of Figure 4. The positive velocity indicates flow towards the free surface and negative towards the bottom of the channel. When the vegetation was non-existent or emergent (cases 0 and 5, respectively), the upstream half of the cavity will have downward flow in the region of contact with the wall, which became upward flow when approaching the center of the cavity. For partial vegetation cases (cases 1 to 4), the velocity profile in the upstream half showed an inversion in the flow in relation to the other two cases, with the regions close to the wall having an upward flow and reverting to a downward flow as the away from the upstream.

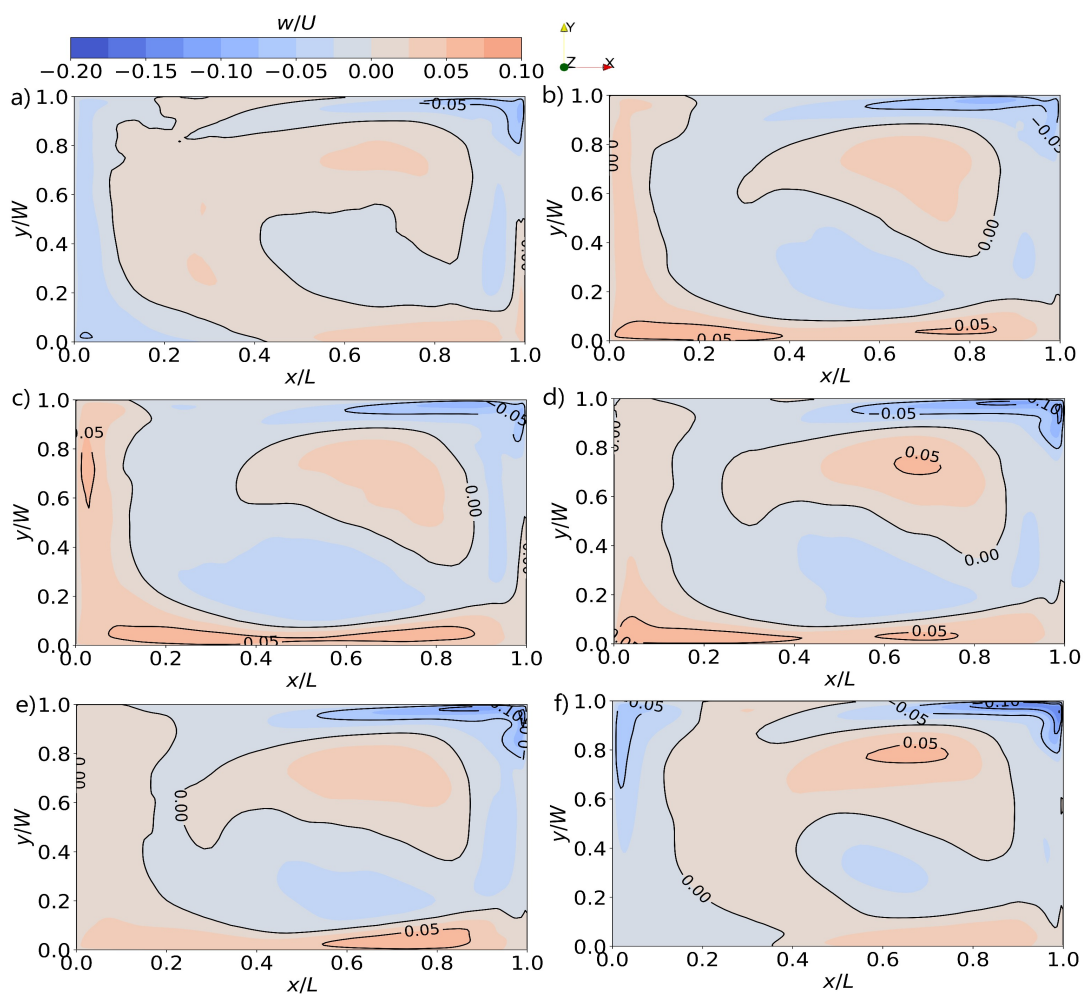


Figure 6 - Velocity contour along the z axis at $z = 0.60H$ in case with floating island bottom with vegetation depth of: a) 0,0H, b) 0.2H, c) 0.4H, d) 0.6H, e) 0.8H and f) 1.0H.

Figures 7 and 8, as well as Figure 6, show the vertical velocity profile inside the cavity for the case without vegetation (case 0) and with floating vegetation down to 0.6m of the depth (case 2), respectively. For cases with resistance exerted by homogeneous vegetation on the vertical axis, the direction of vertical flow remains the same both at depths below $z = 0.6H$ and above. However, in the region closest to the surface, the flow ends up losing speed, especially the upward flow, due to its very proximity to the water layer.

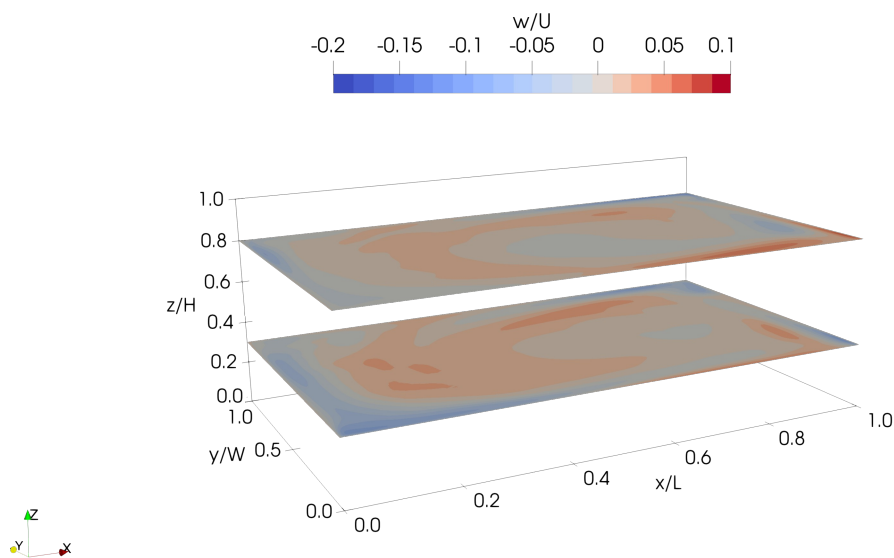


Figure 7 - Velocity contour along the z axis in case without vegetation.

Figure 8 shows that half of the upstream cavity presents the same inversion in flow direction in cases where heterogeneity in flow resistance remains at all depths. The presence of veto only in part of the depth causes this inversion not only at $z = 0.6H$, with only the difference in its magnitude occurring depending on the depth. As in the region closest to the water depth, the flow becomes slower, however, maintaining its direction.

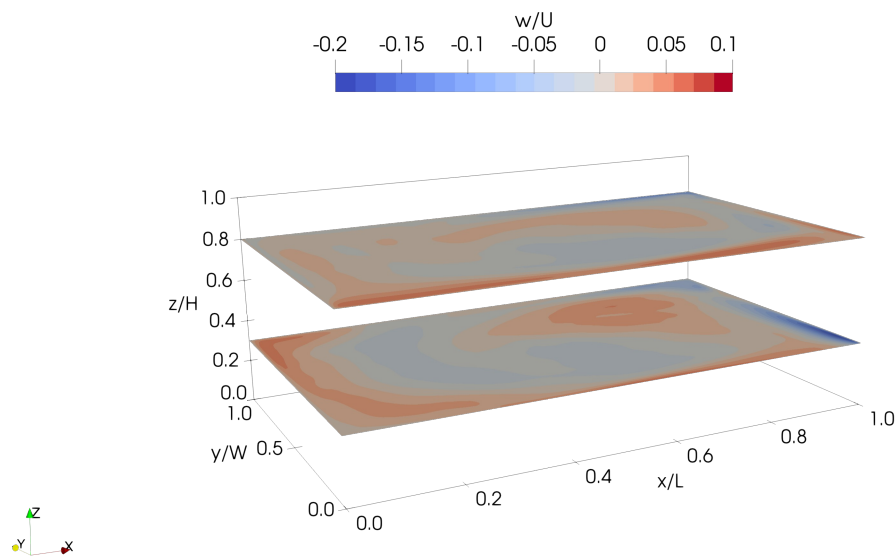


Figure 8 - Velocity contour along the z axis in case with vegetation depth of $0.4H$.

Figure 9 shows the contour of the vertical velocity at the bottom of the Island for cases 1 to 4, at Figure 9 a to d respectively, with flow towards the water sheet having positive values and towards the bottom of the channel having negative values. In cases of floating vegetation, the lack of vegetation throughout the entire depth does not affect the direction of flow, even though the bottom of the island is at different depths in each case. What ended up happening is the difference in magnitude mainly. In some regions with low magnitude flow, there was a change in the flow direction, however, the general flow profile was maintained.

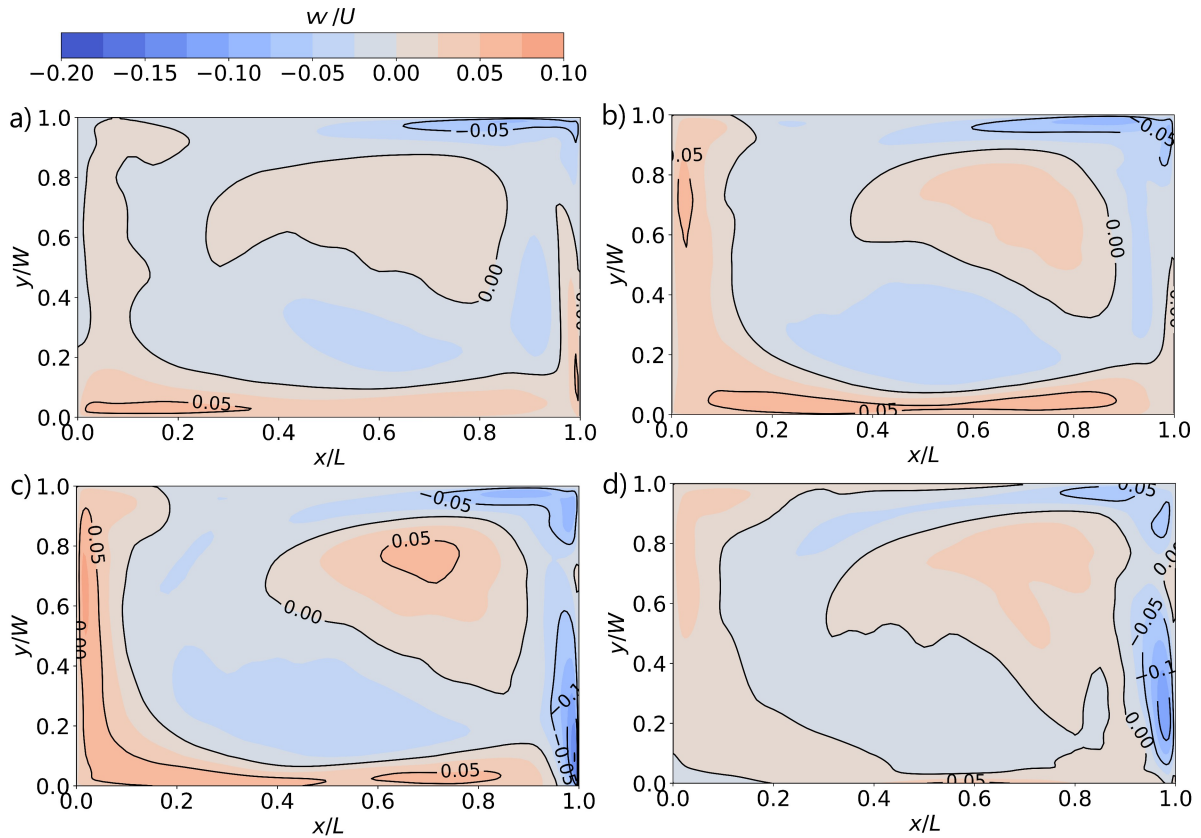


Figure 9 - Contour of the velocity along the z axis in the island bottom with vegetation depth of: a) 0.2H, b) 0.4H, c) 0.6H and d) 0.8H.

Figure 10 shows the vertical velocity through the xz plane at $y = 0.5 W$ (half of the side cavity). Where Figure 10a been the case without vegetation, and having the alphabetical sequence following the sequence of increasing vegetation depth, it also has a red dashed line indicating the bottom of the floating island for the specific case of each contour, condition that is repeated for cases 11 to 13. The plan is able to show how the vertical velocity varies with depth, and thus, explain the inversion in the direction of vertical flow within the cavity in the most upstream half that the partially vegetated cases have. In these cases it is possible to see that the inversion occurs due to the direction of the fortress in this half being clockwise while in homogeneous cases it is counter-clockwise. Furthermore, vegetation also affects the position of the center of the vortex, which tends to be at the bottom interface of the

floating island. As the bottom of the island approaches the bottom of the channel, the center of this vortex moves towards the bottom of the channel, until it reaches 40% of the total depth of the channel where the vegetation no longer influences its position. In addition, floating vegetation generates the formation of another vortex, this one in a counter-clockwise direction in the downstream half of the lateral cavity. Another important issue is to realize that despite having flows with very notable vortices, their flow speed is still very low, being mostly less than 6% of the average speed in the main channel. However, this does not mean that the flow in this region is slow, as seen in Figures 4 and 5, the flow in the xy plane reaches 20% of the speed of the main channel. This is due to the flow in this region occurring mainly on the y axis for all depths.

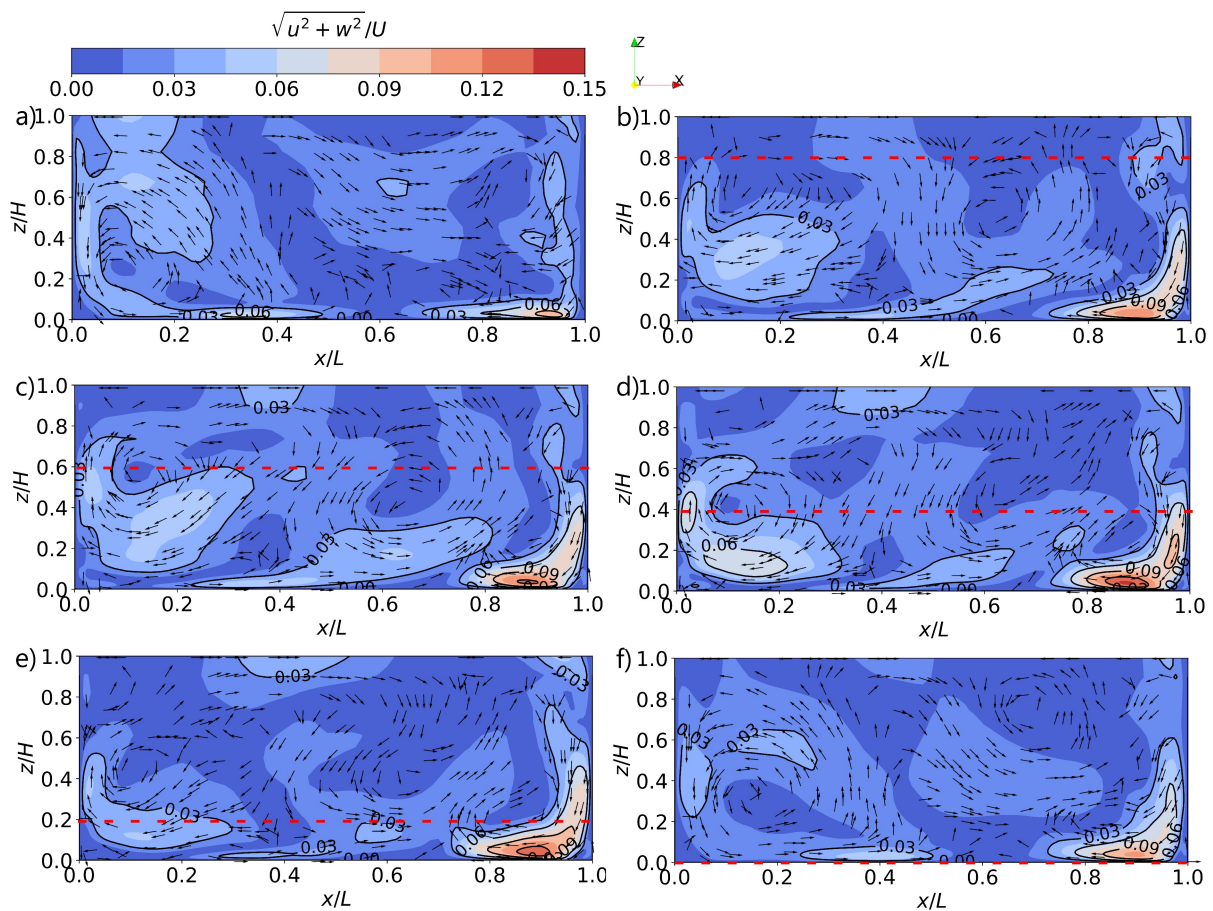


Figure 10 - Superficial velocity contour along the plane xz at $y = 0.5 W$ with vegetation depth of: a) 0.0H, b) 0.2H, c) 0.4H, d) 0.6H, e) 0.8H and f) 1.0H.

Figure 11 shows the flow in the xz plane and, $y = 0.1W$. In this plane, the flow reversal in the most upstream part is already present, however, only in the first 20% of the plane, in the direction of flow in the main channel. In the rest of the plane this inversion does not occur, but it is a region where the main flow is parallel to the free surface and this flow loses energy as the vegetation becomes deeper. The flow only becomes more represented on the axis normal to the free surface in the last 10% of the plane. Although in these more upstream and downstream regions the flow was mainly on the Z axis, the magnitude is much greater in the central region where the flow is mostly on the X axis. This central region is where the flow of greatest magnitude is found, reaching three times faster than in other regions, for cases with less vegetation. However, the region lost energy as the vegetation became deeper, becoming twice as fast as the other two regions for the cases with more vegetation

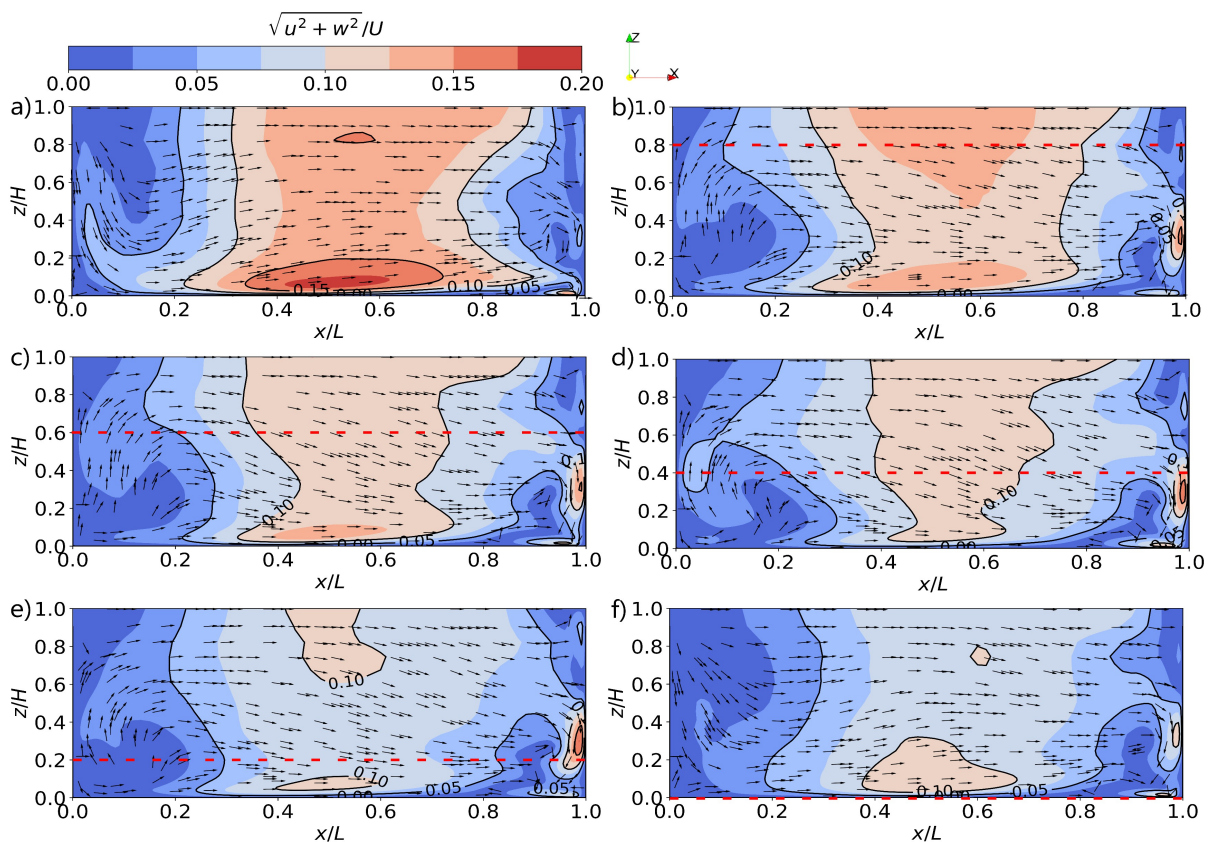


Figure 11 - Superficial velocity contour along the plane xz at $y = 0.1 W$ with vegetation depth of: a) 0.0H, b) 0.2H, c) 0.4H, d) 0.6H, e) 0.8H and f) 1.0H.

Figure 12 shows the flow in the xz axis at the contact interface of the cavity with the main channel. In this region, the most upstream part has lower velocities that gradually increase, reaching their peak at 80% of the length of the cavity where the peak occurs at 65% of the velocity of the main channel. This is due to the influence of the momentum of the main channel that accelerates the flow, making this region have a flow similar to that of the main channel. In other words, being almost unique on the x axis and, as shown in Figures 4 and 5, with the largest magnitude of the cavity. The cases with vegetation partially occupying the depth of the cavity showed a slowdown in flow throughout the region at $z = 0.2H$, independent of the presence of vegetation in the region. A region that ended up returning to being similar to the non-vegetated case when the vegetation became emergent. In addition, the presence of vegetation favors an acceleration in the region above $z = 0.6H$.

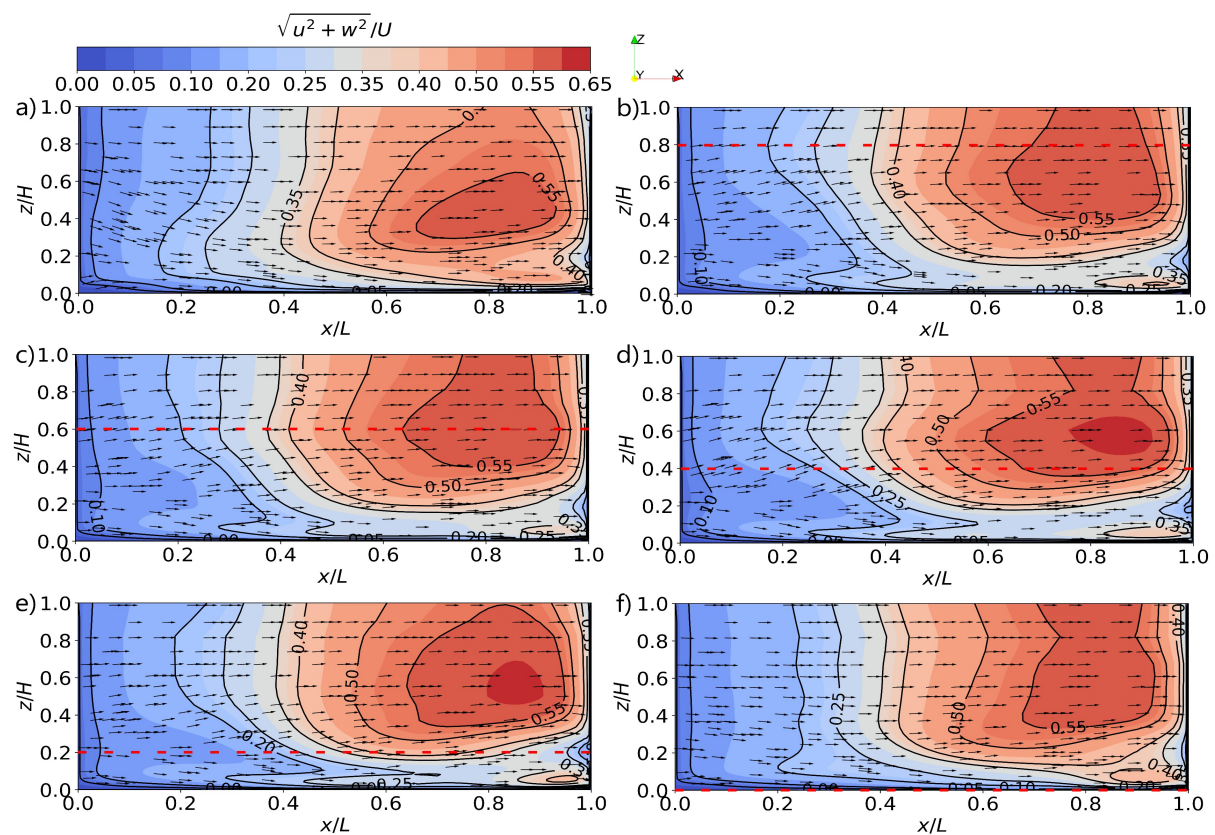


Figure 12 - Superficial velocity contour along the plane xz at the interface with vegetation depth of: a) 0,0H, b) 0.2H, c) 0.4H, d) 0.6H, e) 0.8H and f) 1.0H.

Figure 13 shows the velocity in the Y axis in the plane of the side cavity-main channel interface. In other words, it is the contour of the velocity at the entrance and exit of the cavity, where positive values indicate the velocity at entry into the cavity and negative values at the exit. In addition, it has red dashed lines indicating the vegetation level for each case, so the alphabetical sequence follows the numerical sequence of the cases. For all cases the main zone of both entry and exit is in the downstream half of the interface. This is characterized by a large entry zone, but with low speed, and a small exit zone very close to the wall with a greater magnitude of speed. Another striking aspect is the presence in cases with homogeneous resistance (cases 0 and 1), mainly the case without vegetation, where there is a low-speed entry zone in the upstream half. On the other hand, in cases of floating vegetation there is the emergence of an exit zone in the part close to the region at the bottom of the channel, a little above a region where the flow exits, which disappears again when the vegetation becomes emergent. When carrying out a joint analysis with Figure 12, it can be seen that the region with the highest input velocity is also the region where there is the highest magnitude of velocity on the X axis due to the influence of the main channel. Therefore, the flow that gains speed due to the influence of the main channel, when it gets close to the wall, encounters a physical resistance generated by it, which directs the flow at high speed into the cavity. However, it is important to highlight that the flow is still mostly on the x-axis, where the flow is 3 times faster than on the y-axis. The small exit region, but of high magnitude, close to the upstream wall is due to the flow that breaks away from the vortex, as shown in Figures 4 and 5. Upon reaching the wall opposite the main channel interface, part of the flow was directed to the opposite side of the center of the vortice, with nowhere to go other than the interface region, the flow is directed

there. As there is not much space for flow, there is an increase in pressure which leads to an increase in speed that is up to 25% faster than the fastest inlet region.

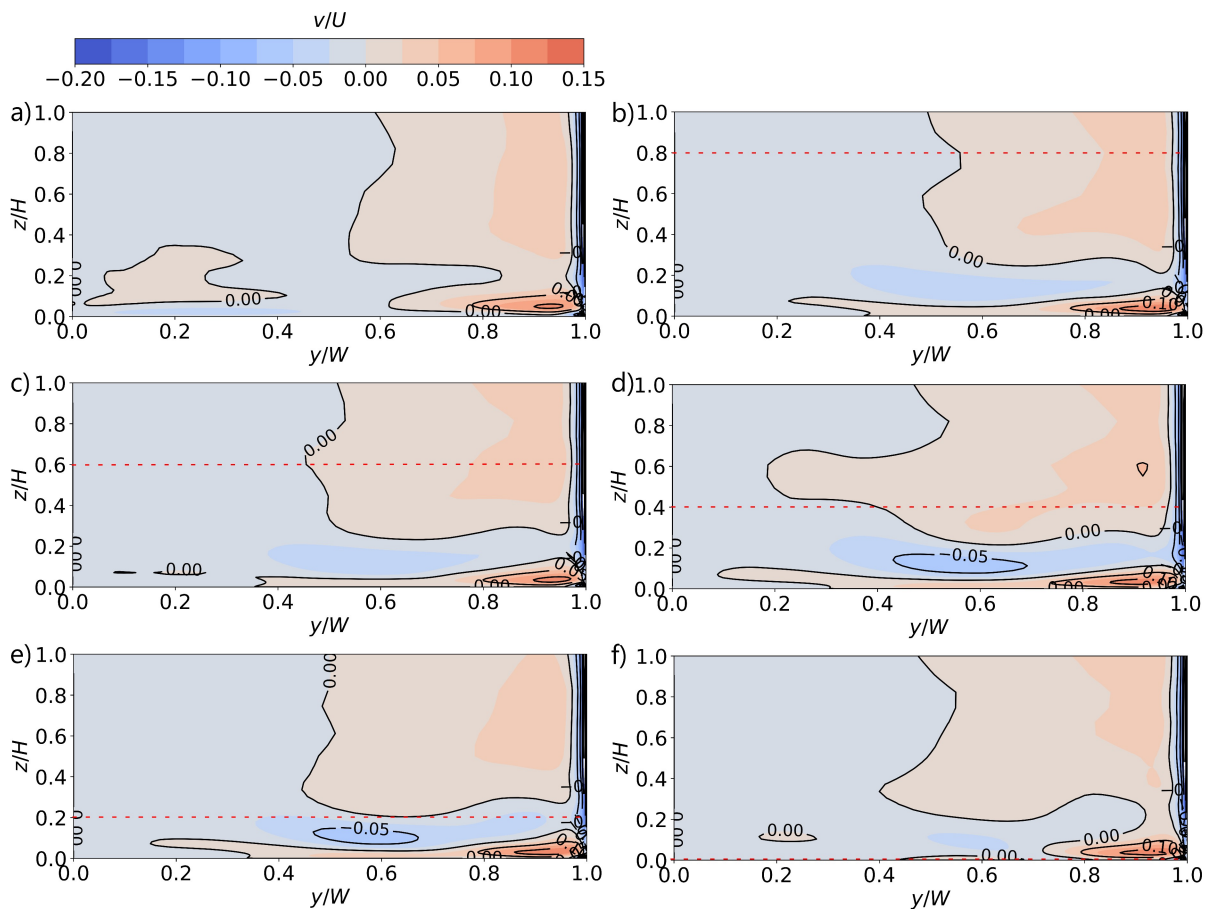


Figure 13 - Contour of the velocity along the y axis in the interface at cases with vegetation depth of: a) 0.0H, b) 0.2H, c) 0.4H, d) 0.6H, e) 0.8H and f) 1.0H.

To better understand the effect of floating vegetation within the lateral cavity, it is important to understand, in addition to the velocity profile within the cavity, the effect that vegetation has on the mass exchange that occurs within the vegetated region and within the cavity as a whole. For this, the analysis of the concentration of a tracer was carried out using figure 14, which presents the graph of the volumetric concentration within the vegetated region by the dimensionless time, this being the time (t_d) times the average velocity in the main channel (U) divided by the cavity width (W). The tracer used was water, as in the rest of the domain, and was released

after the flow had been fully developed. It was placed within the entire volume within the vegetated region and so this volume was the initial concentration of 1.0. Vegetation being emergent generates the case where the tracer concentration presents the slowest drop among all vegetation root depths. Among cases of floating vegetation, cases with shallower vegetation show a more pronounced drop in tracer concentration within the island, a value that ends up being inversely proportional to the depth of the roots. Therefore, the deeper the bottom of the island, the greater the retention capacity the island had.

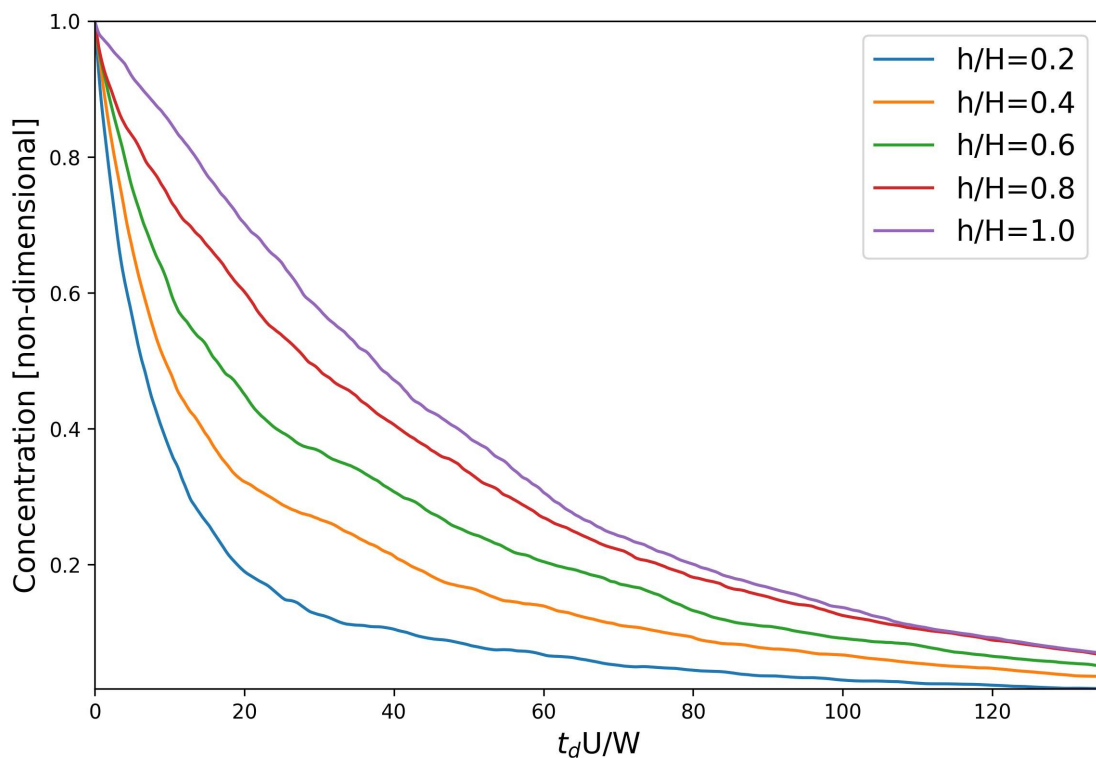


Figure 14 - Volumetric-averaged tracer concentration decay inside the vegetation over time.

Table 2 shows a comparison of tracer concentrations for the different vegetated cases. The comparison was made across the areas below the concentration lines using the emerging case as a reference. The emerging case was considered as a 100% area and the other cases were compared by how many percent each area occupied of the reference area. The linear increase in vegetation depth did not result

in a linear increase in the volume of tracer maintained within the vegetation. The first increase of 20% in depth resulted in an increase of 4.4% while the last increase of 20% resulted in a 21.5% increase in the percentage of mass maintained within the vegetation. However the intermediate values there was a constant increase Since both the second increase and the third increase in depth generated an increase of around 15.75%. The initial slow increase in mass retention is due to the minimum amount that vegetation is capable of retaining, however, once the vegetation passes 40% of the total depth it ends up being able to increase its mass retention. From the moment the vegetation reaches intermediate depths (from 40 to 80% of the total depth of the cavity) the vegetation showed a high acceleration with an increase in the retention variation. When starting to reach the bottom of the channel (from 80% of the depth) the mass exchange started to occur mainly with the main channel and no longer in non-vegetated regions as it began to become insistent.

h/H	Area (%)
0.2	32.6
0.4	37.0
0.6	52.5
0.8	68.5
1.0	100

Table 2 - Volumetric concentration comparison for all vegetated cases.

To have another view of the mass concentration within the Island, Figure 15 grouped the average retention time (T_d) for each case. When comparing the average concentration times, it was noticed that as the vegetation became deeper, the average concentration time increased. The average retention time showed a linear increase until reaching its maximum value when the roots reached the bottom of the cavity. The final value presented a value similar to the non-vegetated case, an event

that occurred due to low vegetation density. Added to this, when compared to the results in Figure 14, it is clear that despite the considerable difference between the retention times of case with vegetation depth of 0.2H in relation to case with vegetation depth of 1.0H, it is clear that the big difference is in the initial moments. Although there was a large difference in the initial concentration values, over time these values became increasingly closer. Similarity that occurs mainly when the vegetation is already deep, above 60% of the channel depth.

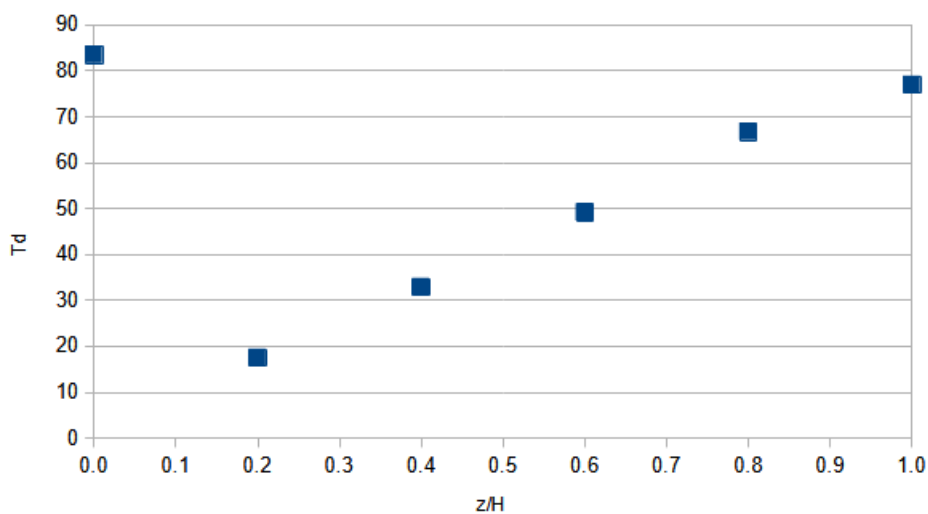


Figure 15 - Mean Retention time for all cases.

In addition to analyzing volumetric flow of mass, it is also important to understand where this mass leaves the vegetated region. Therefore, Figure 16 shows the concentration of the tracer on the side of the Island in contact with the main channel-cavity interface. For all cases of floating vegetation a sharp drop in concentration occurs initially as well as the total volume. However, a case of reflux ends up occurring in this region, an event that ends up dividing the cases into two groups based on the moment of reflux. The first group are cases where the bottom of the island is above 50% of the total depth of the channel, cases in which the main reflux ends up occurring earlier. The second group where the cases with the bottom of the

Island fit is below half of the channel, this reflux process ends up being delayed and peaking later. Despite initially not showing a relationship with the depth of the islands, after increases in concentration, the greater depth of the vegetation generates less mass outflow from the side of the island.

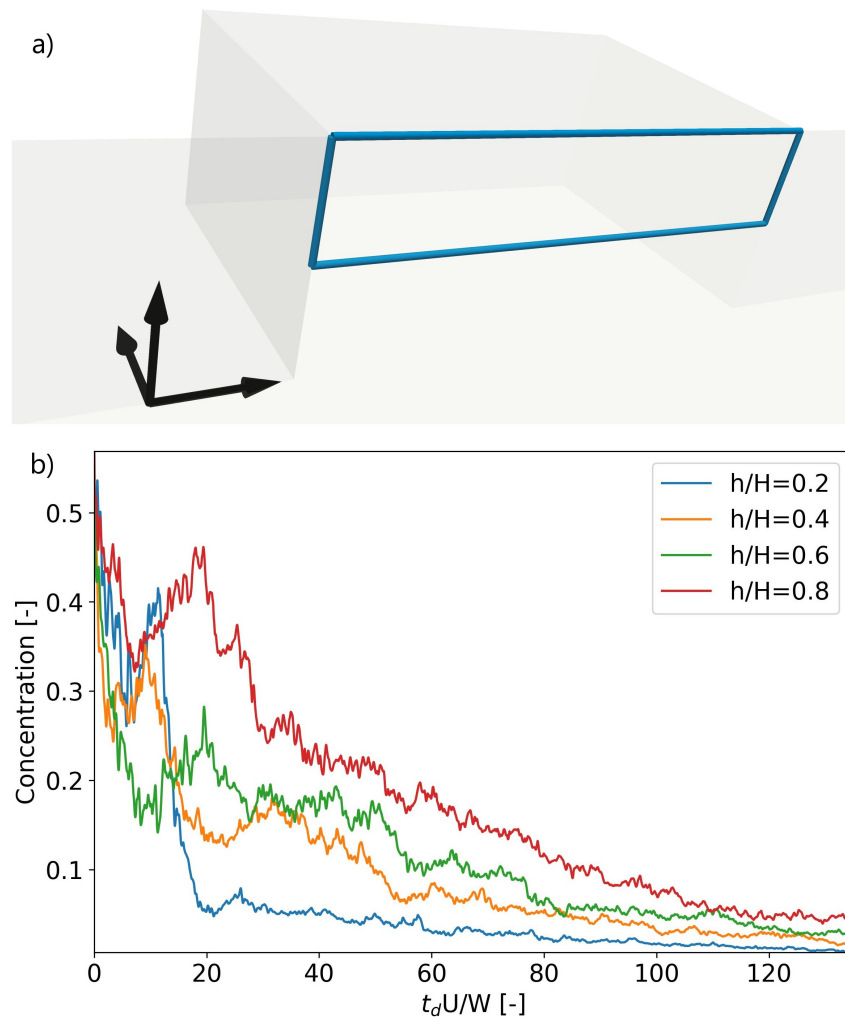


Figure 16 - a) Region of analyses and b)Tracer concentration decay in the lateral of the island over time.

To continue with the analysis, Figure 17 repeated the same control as Figure 16, however, this time for the bottom region of the islands. In this case, a simpler behavior occurred where there was mainly a gradual drop in concentration for all cases, however, just like the side of the Island there was a cluster and a separation

between two groups. The first group is for cases where the bottom of the Island is above half the depth of the channel, where no mass reflux occurs. While the second are cases where the bottom of the island is below 50% of the total depth, where a mass reflux occurs, although smaller than on the lateral of the island.

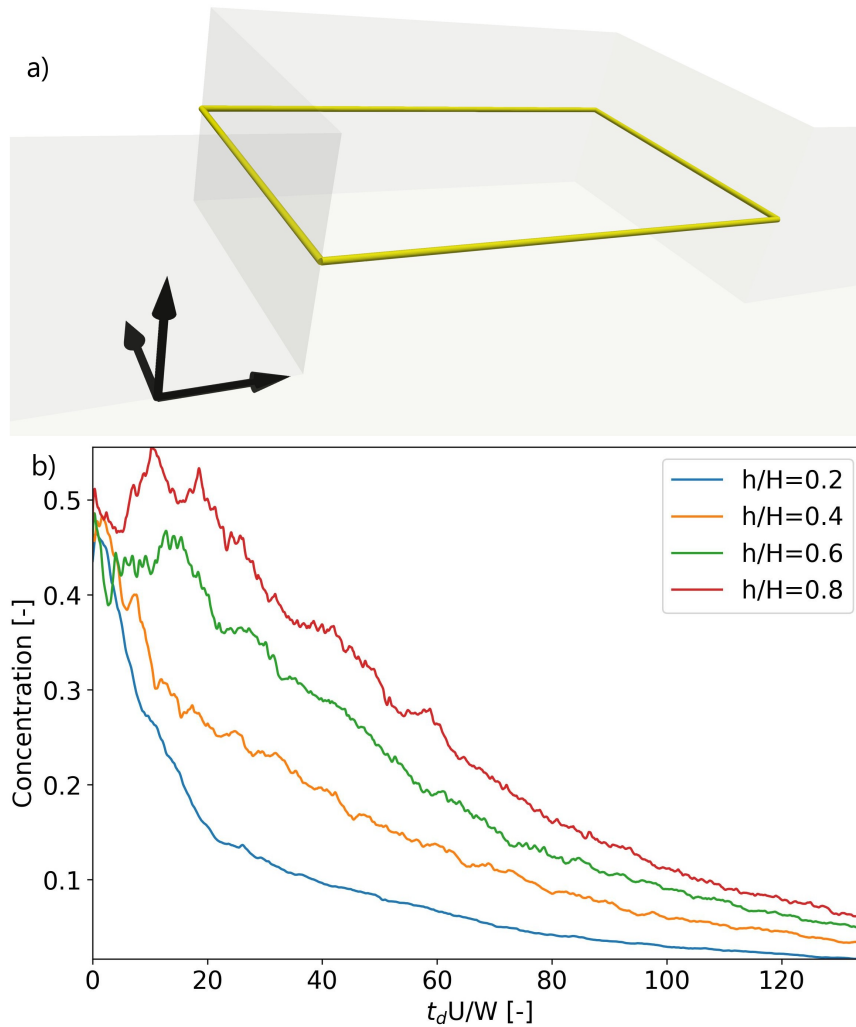


Figure 17 - a) Region of analyses and b)Tracer concentration decay in the bottom of the island over time.

As well as the two previous figures, Figure 18 shows the tracer concentration in a region of the cavity, however, this time in the interface region below the floating vegetation. In this case, there was initially an increase in concentration due to the initial lack of tracer presence, but it initially leaves the island through the bottom of

the island and eventually leaves the cavity through the interface region below the vegetation level. Just like the two previous regions, there was a division of cases into two groups, however, different from previous cases where the division was between cases with vegetation below or above half the total depth. In this region, the mass flow behavior divided the cases into groups separated by the difference in depth between the vegetated and non-vegetated regions. The first group is for cases where the ratio between the depth of the predominant region in relation to the non-predominant region is less than two, in these cases there is an increase in concentration followed by a gradual decline. The second group is where this ratio is greater than two, in this group the same increase occurs, however, it reaches a peak that is followed by an abrupt drop in concentration and finally presents the same gradual falling behavior.

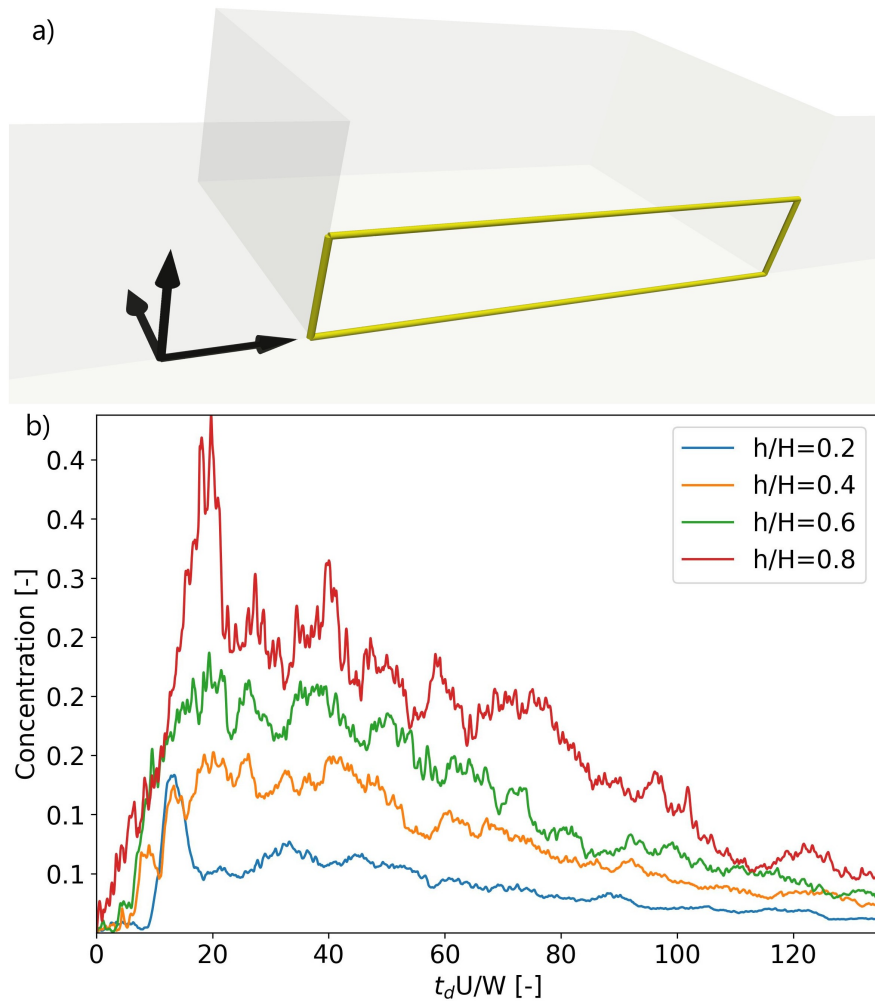


Figure 18 - a) Region of analyses and b)Tracer concentration decay in the interface below the island over time.

In order to understand the behavior of the mass flow for the groups presented in Figures 16 and 1, Figure 19 groups the concentration for the regions of these figures for the same case. Initially analyzing only the case where the vegetation is above half the total depth, using case 1 as an example. In this group, a reflux occurred on the lateral region of the island, however, it was not accompanied by any variation in the concentration of mass exchange at the bottom. of the Island, which indicates that this increase is due to a local event.

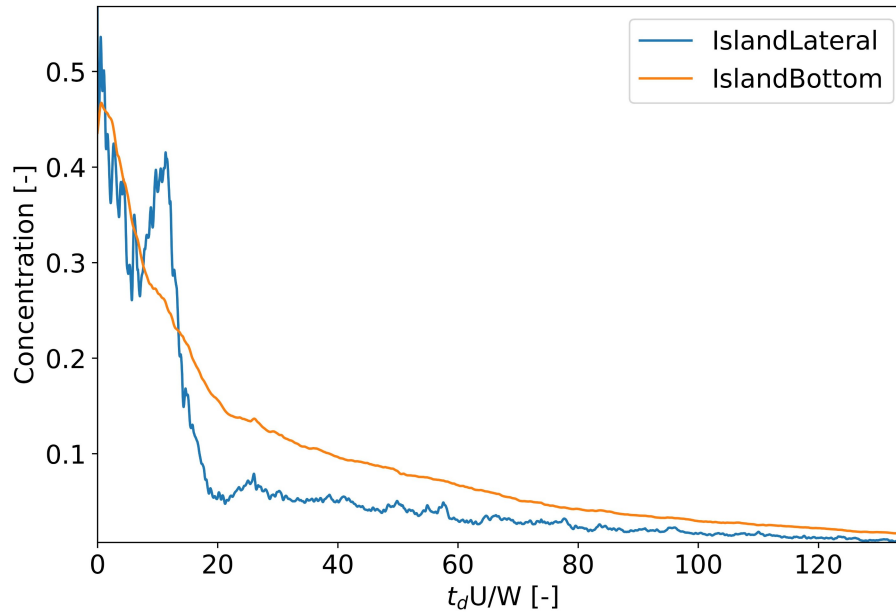


Figure 19 - Tracer concentration decay in the lateral and the bottom of the island over time in case 1.

Figure 20 repeats the same group of data as figure 19, however, this time for the second group that presents vegetation below 50% of the total depth of the channel. In this group, the peak on the side of the island is later and also has a peak at the bottom of the island. The increase in concentration at the bottom of the island occurred slightly before the lateral increase, in addition to the same sequence occurring at the end of the increase.

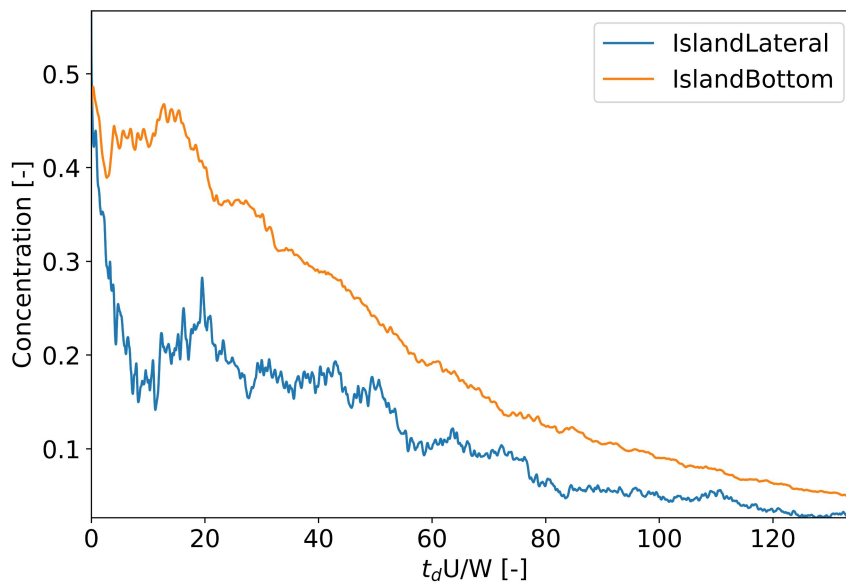


Figure 20 - Tracer concentration decay in the lateral and the bottom of the island over time in case 3.

In order to understand the tracer behavior at the interface below the Island, Figure 21 was generated showing the tracer concentration in this region and in the upper region of the interface (region in contact with the side of the Island). The figure shows the result of case 2, the case of the group with the ratio between the greatest depth of the predominant region, between the vegetated and non-vegetated region, and the non-predominant one is less than two. In these cases, after the increase in concentration, a decay occurred that, upon reaching similar levels in the lower region of the interface, resulted in a subtle increase in concentration in the upper region of the interface, but still remained at similar levels of concentration in the lower part of the interface. Similarity was maintained from this moment on due to the dispersion of the tracer throughout the cavity.

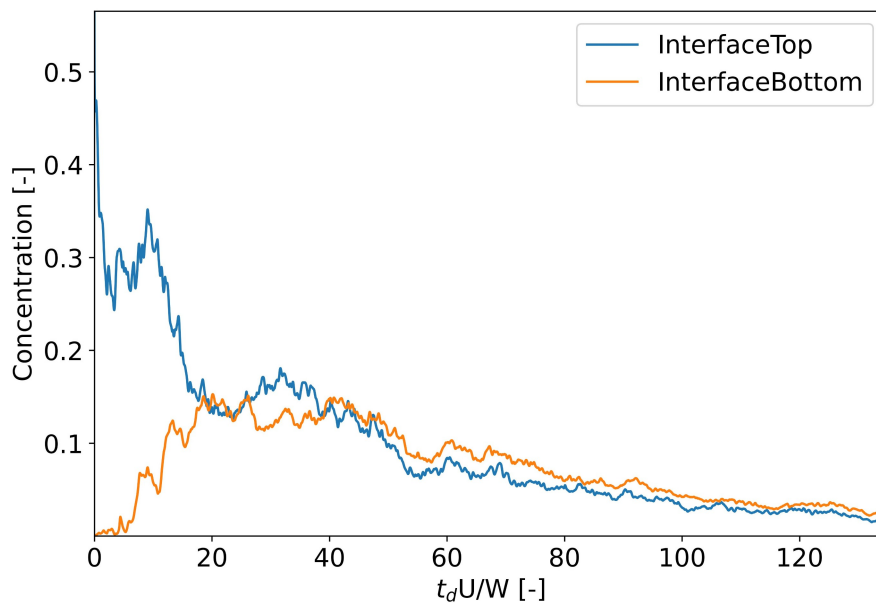


Figure 21 - Tracer concentration decay on the interface over time in case 2.

Just like Figure 21, Figure 22 shows the concentration at the interface separating between the lower region (region where there is no vegetation) and the upper region (region in contact with the side of the Island), however, now for cases where the ratio between the predominant and non-predominant area is greater than two. Using case

4 as an example, this group of cases has the reflux peak in the upper region at the same time as the peak in the lower region of the interface. The concentration then follows a similar decay for both regions, showing that the tracer spreads throughout the cavity regardless of the depth of the vegetation. Although the cases with vegetation depth at $0.2H$ and $0.8H$ have the tracer output peak through the interface region below the vegetated region, this event is not due to a similarity between the cases. In the case with vegetation up to a depth of $0.2H$, the tracer ends up having an increase with a well-marked peak, and the abrupt drop is due to the end of the mass. The end of the tracer is as shown in Figure 14 where only 20% of the tracer remains within the vegetation, while the next case with less tracer has more than 35%, and its output becomes much lower after that point. In the case with vegetation at $0.8H$, it is due to the cavity flow itself. In figures 10 to 12 it was possible to see that the main mass exchange between the vegetated and non-vegetated region occurred far from the interface and mainly in the central region of the cavity. Added to this, this was a region with flow in the direction of the interface, as shown in Figures 4 and 5, and in Figure 13 it is shown that this central region and below the vegetation has mainly outflow flow. The end of the peak is due to the spread of the tracer throughout the cavity as a whole, which favors a more homogeneous exit of the tracer.

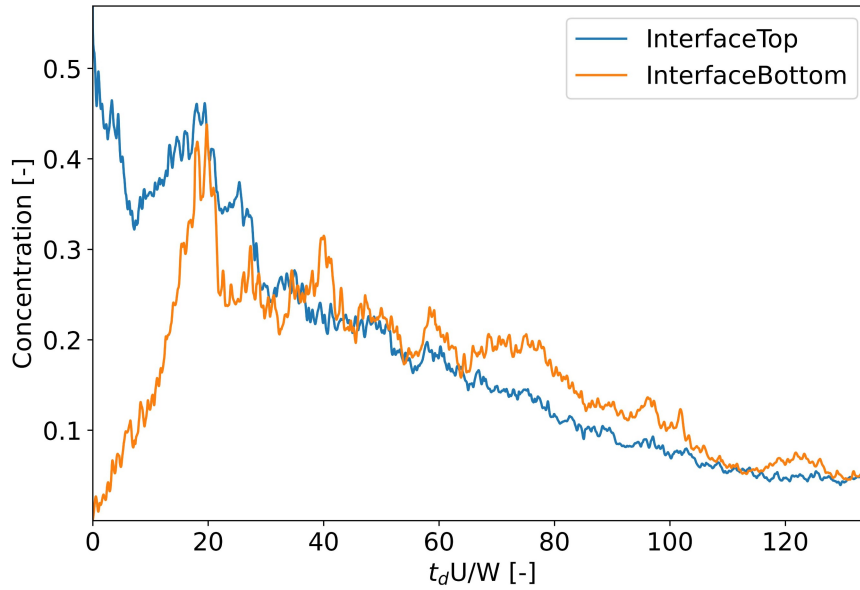


Figure 22 - Tracer concentration decay on the interface over time in case 4.

4. Conclusion

The presence of a floating island results in a significant change in the flow behavior within a cavity, in addition to the influence of floating vegetation ending up being very different from the effect of emerging vegetation. The emerging case presents characteristics more similar to the non-vegetated case than to the cases of floating vegetation, only varying the magnitude of the flow while the cases of floating vegetation result in variation even in the direction of the flow. The difference is mainly due to the different resistance to flow within the cavity since the vegetation exists only in a portion of the upper part. However, the effect generated is mainly in the flow in the Z axis (flow towards the free surface or the bottom of the channel) and not so much in the flow in the plane parallel to the free surface.

In mass exchange, the effect of vegetation follows an increasing trend as the depth of vegetation increases. Even if the increase is not linear, it is possible to separate it

into groups, where vegetation occupying less than 40% of the total area has similar values, from 40 to 80% a constant increase and occupation above 80% has an accelerated increase.

Furthermore, for the practical application of vegetation, it is interesting to understand what effect of vegetation is desired in order to choose the best depth for each project. This is important since the partial presence of vegetation in the z-axis generates different flow behaviors, especially in the z-axis itself, and some of the effects of vegetation are lost when the vegetation reaches the bottom of the channel, such as when specific zones of flow rise and fall are desired. .

An example is if the speed profile of cases with floating vegetation is what you want, it is worth initially installing shallower islands, around 20% of the total depth, and only carrying out maintenance when they reach 80% to prevent them from losing their effect when they reach the bottom. However, if the vegetation also has the function of mass retention, it would not be good to use vegetation as shallow as 20%, and it is better to always keep it below 40%, which is the depth range that has the greatest increase in mass retention, but without leaving until the vegetation reaches the bottom. However, if the focus is only on mass retention, greater depths are more advisable, just being careful with the increase in vegetation density, which may have undesired effects.

A final important addendum is that for future studies, a point that is important to analyze is the chemical effect of vegetation on mass exchange. This point is important, as real vegetation presents chemical processes to obtain nutrients and thus generate treatment for pollutants that enter the cavity region. The study is probably important since mass retention ends up not being linearly related to depth and, therefore, the treatment probably won't be either.

Declaration of Competing Interest

The authors have no conflicts of interest directly relevant to the content of this article.

Acknowledgements

The present study was carried out under the financial supports from the Coordenação de Aperfeiçoamento de Pessoal de Nível Superior – Brazil (CAPES) – Finance Code 001, CAPES - Institutional Internationalisation Programme (Print) and the computational time granted at Lobo Carneiro cluster located in NACAD/Coppe - Rio de Janeiro, Brazil.

Felipe R. da Costa received scholarship from Coordination for the Improvement of Higher Education Personnel (CAPES), number 88887.675525/2022-00

References

- Asaeda, T., Siong, K., Kawashima, T., Sakamoto, K., 2009. Growth of *Phragmites japonica* on a sandbar of regulated river: Morphological adaptation of the plant to low water and nutrient availability in the substrate. *River Res Appl* 25, 874–891. <https://doi.org/10.1002/rra.1191>
- Brevis, W., García-Villalba, M., Niño, Y., 2014. Experimental and large eddy simulation study of the flow developed by a sequence of lateral obstacles. *Environmental Fluid Mechanics* 14, 873–893. <https://doi.org/10.1007/s10652-013-9328-x>
- Chen, Z., Ortiz, A., Zong, L., Nepf, H., 2012. The wake structure behind a porous obstruction and its implications for deposition near a finite patch of emergent vegetation. *Water Resour Res* 48. <https://doi.org/10.1029/2012WR012224>
- de Lima, P.H.S., Janzen, J.G., Nepf, H.M., 2015. Flow patterns around two neighboring patches of emergent vegetation and possible implications for deposition and

vegetation growth. *Environmental Fluid Mechanics* 15, 881–898. <https://doi.org/10.1007/s10652-015-9395-2>

de Oliveira, L.E.D., Janzen, J.G., 2020. Mass Exchange in Dead Water Zones: A Numerical Approach, in: Leal Filho, W., de Andrade Guerra, J.B.S. (Eds.), *Water, Energy and Food Nexus in the Context of Strategies for Climate Change Mitigation*. Springer International Publishing, Cham, pp. 59–68. https://doi.org/10.1007/978-3-030-57235-8_5

Dutta, R., Xing, T., 2018. Five-equation and robust three-equation methods for solution verification of large eddy simulation. *Journal of Hydrodynamics* 30, 23–33. <https://doi.org/10.1007/s42241-018-0002-0>

Gualtieri, C., Jiménez, L., & Rodríguez, J. (2010, May). Modelling turbulence and solute transport in a square dead zone. In *1st European IAHR Congress, Edinburgh (Gran Bretagna)*. May (Vol. 4, No. 6).

Harvey, J., Gooseff, M., 2015. River corridor science: Hydrologic exchange and ecological consequences from bedforms to basins. *Water Resour Res* 51, 6893–6922. <https://doi.org/10.1002/2015WR017617>

Harvey, J.W., 2016. Hydrologic Exchange Flows and Their Ecological Consequences in River Corridors, in: Jones, J.B., Stanley, E.H. (Eds.), *Stream Ecosystems in a Changing Environment*. Academic Press, Boston, pp. 1–83. <https://doi.org/10.1016/B978-0-12-405890-3.00001-4>

Jackson, T.R., Haggerty, R., Apte, S. v., 2013. A fluid-mechanics based classification scheme for surface transient storage in riverine environments: Quantitatively separating surface from hyporheic transient storage. *Hydrol Earth Syst Sci* 17, 2747–2779. <https://doi.org/10.5194/hess-17-2747-2013>

Jones, R.C., 2020. Recovery of a Tidal Freshwater Embayment from Eutrophication: a Multidecadal Study. *Estuaries and Coasts* 43, 1318–1334. <https://doi.org/10.1007/s12237-020-00730-3>

Juez, Carmelo, Bühlmann, I., Maechler, G., Schleiss, A.J., Franca, M.J., 2018. Transport of suspended sediments under the influence of bank macro-roughness. *Earth Surf Process Landf* 43, 271–284. <https://doi.org/10.1002/esp.4243>

Juez, C., Thalmann, M., Schleiss, A.J., Franca, M.J., 2018. Morphological resilience to flow fluctuations of fine sediment deposits in bank lateral cavities. *Adv Water Resour* 115, 44–59. <https://doi.org/10.1016/j.advwatres.2018.03.004>

Kara, S., Kara, M.C., Stoesser, T., Sturm, T.W., 2015. Free-Surface versus Rigid-Lid LES Computations for Bridge-Abutment Flow. *Journal of Hydraulic Engineering* 141, 04015019. [https://doi.org/10.1061/\(asce\)hy.1943-7900.0001028](https://doi.org/10.1061/(asce)hy.1943-7900.0001028)

Kim, H.S., Kimura, I., Shimizu, Y., 2015. Bed morphological changes around a finite patch of vegetation. *Earth Surf Process Landf* 40, 375–388. <https://doi.org/https://doi.org/10.1002/esp.3639>

- King, A.T., Tinoco, R.O., Cowen, E.A., 2012. A k - ϵ turbulence model based on the scales of vertical shear and stem wakes valid for emergent and submerged vegetated flows. *J Fluid Mech* 701, 1–39. <https://doi.org/10.1017/jfm.2012.113>
- Lu, J., Dai, H.C., 2016. Large eddy simulation of flow and mass exchange in an embayment with or without vegetation. *Appl Math Model* 40, 7751–7767. <https://doi.org/10.1016/j.apm.2016.03.026>
- Maceina, M.J., Slipke, J.W., Grizzle, J.M., 1999. Effectiveness of Three Barrier Types for Confining Grass Carp in Embayments of Lake Seminole, Georgia. *N Am J Fish Manag* 19, 968–976. [https://doi.org/10.1577/1548-8675\(1999\)019<0968:eotbtf>2.0.co;2](https://doi.org/10.1577/1548-8675(1999)019<0968:eotbtf>2.0.co;2)
- McCoy, A., Constantinescu, G., Weber, L., 2007. A numerical investigation of coherent structures and mass exchange processes in channel flow with two lateral submerged groynes. *Water Resour Res* 43, 1–26. <https://doi.org/10.1029/2006WR005267>
- Mignot, E., Cai, W., Riviere, N., 2019. Analysis of the transitions between flow patterns in open-channel lateral cavities with increasing aspect ratio. *Environmental Fluid Mechanics* 19, 231–253. <https://doi.org/10.1007/s10652-018-9620-x>
- Nicoud, F., Ducros, F., 1999. Subgrid-scale stress modelling based on the square of the velocity gradient tensor. *Flow Turbul Combust* 62, 183–200. <https://doi.org/10.1023/A:1009995426001>
- Oldham, C.E., Sturman, J.J., 2001. The effect of emergent vegetation on convective flushing in shallow wetlands: Scaling and experiments. *Limnol Oceanogr* 46, 1486–1493. <https://doi.org/10.4319/lo.2001.46.6.1486>
- Olesen, B., 1996. Regulation of light attenuation and eelgrass *Zostera marina* depth distribution in a Danish embayment. *Mar Ecol Prog Ser* 134, 187–194. <https://doi.org/10.3354/meps134187>
- Oliveira, L., Queiroz, F., Yamasaki, T., Janzen, J., Gualtieri, C., 2021. Effects of the Turbulent Schmidt Number on the Mass Exchange of a Vegetated Lateral Cavity, in: *EGU General Assembly 2021*. <https://doi.org/10.5194/egusphere-egu21-5708>
- Ouro, P., Juez, C., Franca, M., 2020. Drivers for mass and momentum exchange between the main channel and river bank lateral cavities. *Adv Water Resour* 137. <https://doi.org/10.1016/j.advwatres.2020.103511>
- Perrot-Minot, C., Mignot, E., Perkins, R., Lopez, D., Riviere, N., 2020. Vortex shedding frequency in open-channel lateral cavity. *J Fluid Mech* 892. <https://doi.org/10.1017/jfm.2020.186>
- Poletto, R., Craft, T., Revell, A., 2013. A new divergence free synthetic eddy method for the reproduction of inlet flow conditions for les. *Flow Turbul Combust* 91, 519–539. <https://doi.org/10.1007/s10494-013-9488-2>
- Rodi, W., Constantinescu, G., Stoesser, T., 2013. *Large-Eddy Simulation in Hydraulics*, 1st ed. CRC Press/Balkema, Leiden.

- Sukhodolov, A., Uijtewaal, W.S.J., Engelhardt, C., 2002. On the correspondence between morphological and hydrodynamical patterns of groyne fields. *Earth Surf Process Landf* 27, 289–305. <https://doi.org/10.1002/esp.319>
- Sukhodolov, A.N., Sukhodolova, T.A., Krick, J., 2017. Effects of vegetation on turbulent flow structure in groyne fields. *Journal of Hydraulic Research* 55, 1–15. <https://doi.org/10.1080/00221686.2016.1211183>
- Weitbrecht, V., 2004. Influence of Dead-Water Zones on the Dispersive Mass Transport in Rivers. *Dissertationsreihe am Institut für Hydromechanik der Universität Karlsruhe (TH). Karlsruhe Institute of Technology, Karlsruhe.* <https://doi.org/10.5445/KSP/1242004>
- Weitbrecht, V., Socolofsky, S. a., Jirka, G.H., 2008. Experiments on Mass Exchange between Groin Fields and Main Stream in Rivers. *Journal of Hydraulic Engineering* 134, 173–183. [https://doi.org/10.1061/\(ASCE\)0733-9429\(2008\)134:2\(173\)](https://doi.org/10.1061/(ASCE)0733-9429(2008)134:2(173))
- Xavier, M.L.M., Janzen, J.G., Nepf, H., 2018. Numerical modeling study to compare the nutrient removal potential of different floating treatment island configurations in a stormwater pond. *Ecol Eng* 111, 78–84. <https://doi.org/10.1016/j.ecoleng.2017.11.022>
- Xiang, K., Yang, Z., Huai, W., Ding, R., 2019. Large eddy simulation of turbulent flow structure in a rectangular embayment zone with different population densities of vegetation. *Environmental Science and Pollution Research* 26, 14583–14597. <https://doi.org/10.1007/s11356-019-04709-x>
- Xiang, K., Yang, Z., Wu, S., Gao, W., Li, D., Li, Q., 2020. Flow hydrodynamics of the mixing layer in consecutive vegetated groyne fields. *Physics of Fluids* 32, 1–22. <https://doi.org/10.1063/5.0006317>
- Yamasaki, T.N., de Lima, P.H.S., Silva, D.F., Preza, C.G. de A., Janzen, J.G., Nepf, H.M., 2019. From patch to channel scale: The evolution of emergent vegetation in a channel. *Adv Water Resour.* <https://doi.org/10.1016/j.advwatres.2019.05.009>